BEILSTEIN JOURNAL OF NANOTECHNOLOGY

Nanotechnology for cross-scale analysis: comprehensive evaluation of water environments

Edited by Yui Sasaki and Tsuyoshi Minami

Imprint

Beilstein Journal of Nanotechnology
www.bjnano.org
ISSN 2190-4286
Email: journals-support@beilstein-institut.de

The *Beilstein Journal of Nanotechnology* is published by the Beilstein-Institut zur Förderung der Chemischen Wissenschaften.

Beilstein-Institut zur Förderung der Chemischen Wissenschaften
Trakehner Straße 7–9
60487 Frankfurt am Main
Germany
www.beilstein-institut.de

BEILSTEIN JOURNAL OF NANOTECHNOLOGY

Electrochemical determination of ciprofloxacin using a MIL-101/reduced graphene oxide-modified electrode

Nguyen Quang Man[1], Nguyen Ngoc Nghia[*2,3], Nguyen Vinh Phu[1], Vo Thi Khanh Ly[1], Le Lam Son[2], Pham Khac Lieu[2], Le Thi Hong Phong[4], Nguyen Dinh Luyen[5] and Dinh Quang Khieu[*2]

Full Research Paper

Open Access

Address:
[1]University of Medicine and Pharmacy, Hue University, 530000, Vietnam, [2]University of Sciences, Hue University, 530000, Vietnam, [3]Department of Education and Training, Hue City, 530000, Vietnam, [4]Institute of Materials Sciences, Vietnam Academy of Science and Technology, 18 Hoang Quoc Viet, Cau Giay, Hanoi City,100000, Vietnam and [5]University of Education, Hue University, 530000, Vietnam

Email:
Nguyen Ngoc Nghia[*] - nnnghia.al@hue.edu.vn;
Dinh Quang Khieu[*] - dqkhieu@hueuni.edu.vn

* Corresponding author

Keywords:
ciprofloxacin; electrochemical analysis; MIL-101; reduced graphene oxide

Beilstein J. Nanotechnol. **2026,** *17,* 541–554.
https://doi.org/10.3762/bjnano.17.35

Received: 08 January 2026
Accepted: 02 April 2026
Published: 21 April 2026

This article is part of the thematic issue "Nanotechnology for cross-scale analysis: comprehensive evaluation of water environments".

Guest Editors: Y. Sasaki and T. Minami

Abstract

An electrochemical sensor for the determination of ciprofloxacin (CPR) was developed using a glassy carbon electrode modified with MIL-101/reduced graphene oxide (MIL-101/rGO). MIL-101/rGO was synthesized via a facile ultrasonic-assisted method and characterized by various physicochemical techniques. The synergistic combination of MIL-101 with rGO significantly enhanced the electrocatalytic activity toward CPR oxidation. The electrochemical behavior of CPR on the MIL-101/rGO-modified electrode was systematically investigated using cyclic voltammetry and differential pulse voltammetry. Under optimized experimental conditions, the proposed sensor exhibited a linear response over 0.25–9.41 μM and a detection limit of 0.11 μM for CPR determination. The sensor also demonstrated good selectivity, satisfactory repeatability, and long-term stability. Furthermore, the method's practical applicability was validated by the determination of CPR in pharmaceutical samples, yielding acceptable recoveries. These results indicate that the MIL-101/rGO-modified electrode provides a promising and efficient platform for the electrochemical sensing of CPR in pharmaceutical and environmental analysis.

Introduction

Ciprofloxacin ($C_{17}H_{18}FN_3O_3$, CPR) is a fluoroquinolone antibiotic widely used in human and veterinary medicine to treat various bacterial infections [1]. Due to its high usage, incomplete metabolism, and environmental persistence, CPR residues are often found in pharmaceutical products, biological fluids, and aquatic environments [2,3]. The uncontrolled presence

of ciprofloxacin not only poses risks to human health but also promotes the development of antibiotic-resistant bacteria, raising significant environmental and public health concerns [4]. Therefore, developing sensitive, selective, and affordable analytical methods for detecting ciprofloxacin is very important.

Conventional analytical techniques for CPR determination, including a fluorescence sensor based on $CsPbBr_3$ quantum dots embedded in a molecularly imprinted polymer [5], and ultrasound-assisted magnetic dispersive micro-solid phase extraction based on carbon quantum dots/zeolite imidazolate framework-90/polyvinyl pyrrolidone/iron(II,III) oxide with high-performance liquid chromatography [6,7] or chromatography–tandem mass spectrometry [8] offer high accuracy and reliability. However, these techniques often need expensive equipment, complex sample preparation, skilled operators, and lengthy analysis times, which restrict their use for quick or in situ testing. In contrast, electrochemical sensors have become appealing alternatives because of their inherent benefits such as simplicity, low cost, rapid response, high sensitivity, and potential for miniaturization and field use.

The performance of electrochemical sensors heavily relies on the electrode's surface properties. Recently, metal–organic frameworks (MOFs) have attracted significant interest in electrochemical sensing due to their highly ordered porous structures, very high surface areas, tunable pore sizes, and numerous active sites. Among these, MIL-101, a chromium-based MOF, is notable for its large pore volume, excellent chemical stability, and strong ability to adsorb organic molecules [9-11].

However, the poor electrical conductivity inherent to MIL-101 limits its direct use in electrochemical sensing. To address this limitation, hybridizing MOFs with conductive carbon materials has been extensively studied. Reduced graphene oxide (rGO) is especially appealing due to its high electrical conductivity [12], large specific surface area, mechanical stability [13], and strong π–π interactions with aromatic compounds like ciprofloxacin [14,15].

Integrating MIL-101 with rGO aims to combine the high surface area and adsorption capacity of MIL-101 with the excellent electrical conductivity and electron-transfer ability of rGO, creating a synergistic effect that boosts the electrochemical performance of the composite material. This combination can promote efficient analyte adsorption and fast charge transfer at the electrode interface. Consistent with this idea, Gu et al. reported that MIL-101/rGO composites exhibit enhanced electrocatalytic activity toward the reduction of metronidazole and the anodic stripping detection of Cd^{2+} and Pb^{2+}, demonstrating a strong synergistic effect between MIL-101 and rGO in electrochemical sensing [16].

In this work, a MIL-101/rGO hybrid was successfully synthesized and used as a modifier for a glassy carbon electrode to develop a sensitive electrochemical sensor for CPR detection. The electrochemical behavior of CPR on the MIL-101/rGO-modified electrode was examined. The proposed sensor demonstrated enhanced electrocatalytic activity, high sensitivity, and a low detection limit for CPR. Additionally, the practical utility of the sensor was confirmed through its application in analyzing real samples, highlighting its potential for pharmaceutical and environmental monitoring.

Experimental

Materials

Ciprofloxacin (CPR) was obtained from a commercial supplier and used without additional purification. Chromium(III) nitrate nonahydrate ($Cr(NO_3)_3{\cdot}9H_2O$), terephthalic acid (H_2BDC), graphite powder, potassium permanganate ($KMnO_4$), sodium borohydride ($NaBH_4$), sulfuric acid (H_2SO_4), hydrogen peroxide (H_2O_2), and other analytical-grade reagents were purchased from standard chemical suppliers. Britton–Robinson (BR) buffer solutions at different pH levels were prepared using a mixture of acetic acid, phosphoric acid, and boric acid, with pH adjusted using 0.2 M NaOH solution.

Synthesis of reduced graphene oxide (rGO), MIL-101, and MIL-101/rGO

Graphene oxide (GO) was synthesized from natural graphite using a modified Hummers' method, as described in [17]. MIL-101(Cr) was prepared through a hydrothermal reaction by dissolving terephthalic acid (H_2BDC, 1.66 g) and chromium(III) nitrate nonahydrate ($Cr(NO_3)_3{\cdot}9H_2O$, 4.0 g) in 48 mL of deionized water, followed by the addition of 2 mL of hydrofluoric acid. The mixture was transferred to a Teflon-lined stainless-steel autoclave and heated at 200 °C for 8 h [18]. After cooling to room temperature, a highly crystalline green chromium terephthalate powder (MIL-101(Cr)) was collected by filtration, thoroughly washed with deionized water, and dried before use.

The MIL-101/rGO composites were synthesized following a reported procedure with slight modifications [18]. Briefly, dried MIL-101(Cr) (0.1 g) was dispersed in 20 mL of deionized water and ultrasonicated for 30 min to obtain a homogeneous suspension. Subsequently, a predetermined amount of GO was added to the MIL-101 suspension under continuous stirring, followed by ultrasonication for 30 min. Sodium borohydride ($NaBH_4$) was then introduced into the mixture, which was heated at

60 °C and stirred continuously for 12 h to reduce GO and form the MIL-101/rGO composite (Table 1).

Table 1: The composition for MIL-101/rGO.

Notation	MIL-101 (mg)	GO (mg)	$NaBH_4$ (mg)
MIL-101/rGO(10)	100	10	35
MIL-101/rGO(5)	100	20	70
MIL-101/rGO(3.3)	100	30	105
MIL-101/rGO(2.5)	100	40	140
MIL-101/rGO(2)	100	50	175

After the reaction was completed, the product was collected by filtration, washed several times with deionized water to remove residual reagents, and dried at 60 °C for 24 h before use. The resulting composites were labeled as MIL-101/rGO(10), MIL-101/rGO(5), MIL-101/rGO(3.3), MIL-101/rGO(2.5), and MIL-101/rGO(2), where the numbers in parentheses indicate the mass ratio of MIL-101 to GO. For comparison, reduced graphene oxide (rGO) was also prepared using the same reduction process without MIL-101.

Equipment

The X-ray diffraction analyses were conducted using a D8 Advance Bruker (Germany). Morphology and elemental mapping were measured with a Hitachi S-4800 FESEM (Japan) equipped with an energy-dispersive X-ray (EDX) system. Raman spectroscopy was performed on an Xplora Plus instrument (Horiba, Japan) with a stimulating light wavelength of 785 nm. Electrochemical impedance spectra (EIS) were recorded using an Autolab PGSTAT302N system. Electrochemical experiments were carried out on a CPA-HH5 workstation (Vietnam). A platinum wire served as the counter electrode, and a glassy carbon electrode was used as the working electrode.

Preparation of the modified electrode

Before modification, the glassy carbon electrode (GCE) was polished successively with alumina slurry (0.05 μm) on a polishing cloth, thoroughly rinsed with deionized water, and sonicated in ethanol and water to remove residual impurities. To prepare the modified electrode, a specific amount of MIL-101/rGO composite was dispersed in deionized water using ultrasonication to create a uniform suspension (1 $mg{\cdot}mL^{-1}$). An aliquot of this suspension (5 μL) was drop-cast onto the cleaned GCE surface and allowed to dry naturally at room temperature to form the MIL-101/rGO-modified electrode. The modified electrode was then gently rinsed with deionized water before conducting electrochemical measurements.

Electrochemical measurements

Electrochemical measurements were conducted using a standard three-electrode setup connected to an electrochemical workstation. Cyclic voltammetry (CV) and differential pulse voltammetry (DPV) were employed to analyze the electrochemical behavior of CPR. All tests took place in BR buffer solution at room temperature under optimized pH conditions. DPV parameters, including accumulation potential (E_{acc}), accumulation time (t_{acc}), pulse amplitude (ΔE), and voltage step (U_{step}), were optimized before conducting the analytical measurements.

Real sample preparation

Pharmaceutical samples containing CPR were prepared by carefully weighing and finely grinding the tablets (or powder for oral suspension). A suitable amount of the powdered sample was dissolved in deionized water and sonicated to ensure complete dissolution. The resulting solution was filtered to remove insoluble excipients and properly diluted with BR buffer (pH 4) before electrochemical analysis. The CPR content in the pharmaceutical samples was measured using the standard addition method.

Data analysis

All electrochemical measurements were performed in triplicate. Calibration curves were constructed from DPV peak currents versus CPR concentrations. The limit of detection (LOD) was calculated based on the formula $3S/b$ where S is the standard deviation of the blank signal (or the standard deviation of the intercept of the calibration curve), and b is the slope of the calibration curve [19]. Repeatability, reproducibility, selectivity, and stability of the sensor were evaluated using relative standard deviation (RSD) values.

Results and Discussion

Materials characterization

Figure 1a presents the XRD patterns of GO, rGO, and pristine MIL-101, while Figure 1b shows the diffraction patterns of MIL-101/rGO composites prepared with different MIL-101/rGO mass ratios (as indicated in parentheses). In Figure 1a, GO exhibits characteristic diffraction peaks at 2θ values of 10.9° and 42.7°, corresponding to the (001) plane, which arise from the increased interlayer spacing caused by abundant oxygen-containing functional groups [20]. After reduction, this peak disappears, and broad reflections centered at 2θ values of 25.8° and 43.1° appear for rGO, attributed to the (002) and (100) planes of graphitic carbon, confirming the successful reduction of GO and partial restoration of the sp^2 carbon network [21].

The XRD pattern of the synthesized MIL-101 shows several characteristic diffraction peaks located at 2θ ≈ 5.2°, 5.6°, 5.9°, 8.1°, 8.4°, 9.1°, 10.3°, 16.5°, and 18.0°, which can be indexed

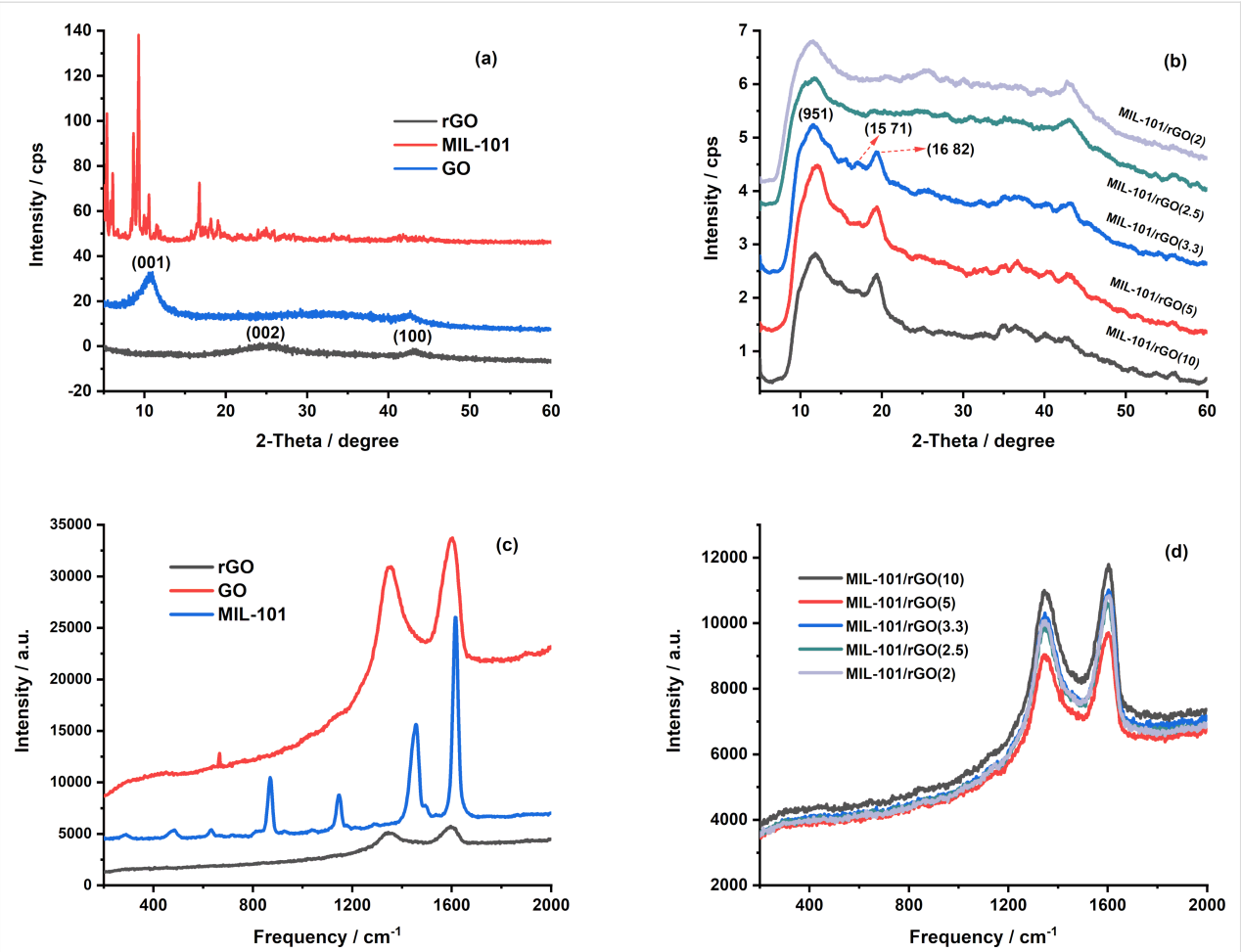

Figure 1: (a) X-ray diffraction (XRD) patterns of graphene oxide (GO), reduced graphene oxide (rGO), and MIL-101, (b) X-ray patterns of MIL-101/rGO with various mass ratios, (c) Raman spectra of GO, rGO and MIL-101, and (d) Raman spectra of MIL-101/rGO with various mass ratios.

to the (333), (440), (442), (733), (660), (911), (951), (15 7 1), and (16 8 2) crystal planes of MIL-101(Cr) according CCCD No. 605510 (Supporting Information File 1, Figure S1) confirming the successful formation of the crystalline MOF framework. As shown in Figure 1b, all MIL-101/rGO composites retain the characteristic angle diffraction peaks of MIL-101 at 2θ = 11.7°, 15.6°, 17.0°, and 19.3°, consistent with [22], indicating that the crystalline framework of MIL-101 remains intact after mixing with rGO, regardless of the mass ratio. Meanwhile, the broad diffraction feature associated with rGO becomes more prominent with increasing rGO content, reflecting the growing contribution of the disordered graphitic phase. The XRD results from both figures confirm the successful formation of MIL-101/rGO composites. This structural combination is beneficial for electrochemical applications because rGO improves electrical conductivity and promotes charge transfer.

The Raman spectra of GO, rGO, MIL-101, and the MIL-101/rGO composites are presented in Figure 1a,c. As shown in Figure 1c, GO exhibits two characteristic bands at ≈1345 cm^{-1} (D band) and ≈1599 cm^{-1} (G band), which are associated with structural defects/disorder and the in-plane vibration of sp^2-bonded carbon atoms, respectively [23]. After chemical reduction, rGO shows a slight shift of these bands to ≈1340 cm^{-1} (D) and ≈1592 cm^{-1} (G), accompanied by an increase in the intensity ratio I_D/I_G from 0.91 (GO) to 0.99 (rGO). This increase indicates the partial restoration of sp^2 carbon domains together with the generation of new, smaller graphitic domains, which is typical for reduced graphene oxide. In contrast, pristine MIL-101 displays multiple Raman bands in the low- and mid-frequency regions (280, 473, 629, 809, 866, 925, 1037, 1145, 1283, 1454, and 1611 cm^{-1}), which can be assigned to lattice vibrations of the metal–oxygen clusters and organic linker modes, confirming the successful formation of the MIL-101 framework [24]. For the MIL-101/rGO composites (Figure 1d), the Raman spectra are dominated by the D and G bands of rGO located at ≈1340 and ≈1600 cm^{-1}, while the characteristic bands of MIL-101 become much weaker or partially over-

lapped due to the strong Raman response of the carbon phase. The I_D/I_G ratios of the composites range from 0.89 to 0.94, depending on the rGO content. Notably, these values are slightly lower than that of pure rGO, suggesting that the incorporation of MIL-101 can partially promote better ordering of sp^2 domains through interfacial interactions between MIL-101 and rGO sheets.

The EDX results confirm the successful formation of the MIL-101/rGO composite through the presence of C, O, and Cr as the main constituent elements. As summarized in the elemental composition table, carbon (C) accounts for 30.42 wt % (42.31 atom %), which mainly originates from the rGO sheets and the organic linker of MIL-101, indicating the effective incorporation of rGO into the composite matrix. Oxygen (O) is the most abundant element with 48.87 wt % (51.03 atom %), consistent with the presence of metal–oxygen clusters in MIL-101 as well as residual oxygen-containing functional groups on rGO. Chromium (Cr), the metal center of MIL-101, is detected at 20.72 wt % (6.66 atom %), confirming the successful introduction of the MIL-101 framework (Figure 2).

The chemical composition and electronic states of the MIL-101/rGO composite were investigated by X-ray photoelectron spectroscopy (XPS). The survey spectrum (Figure 3a) confirms the presence of Cr, C, and O, which is consistent with the expected composition of MIL-101(Cr) integrated with reduced graphene oxide (rGO). No obvious extraneous elemental signals were observed in the survey spectrum, suggesting that the synthesized composite is predominantly composed of the expected elements within the detection limit of XPS. The high-resolution Cr 2p spectrum (Figure 3b) shows two prominent peaks at approximately 577.9 and 589.0 eV, representing the Cr 2p3/2 and Cr 2p1/2 spin–orbit components, respectively. The energy gap between these peaks (≈11.1 eV) is typical of Cr^{3+} species coordinated with oxygen in the Cr–O clusters of the MIL-101 framework [25]. Importantly, no signals related to Cr^{6+} species (usually observed at higher binding energies) are detected, confirming that chromium remains mainly in the trivalent oxidation state. This indicates that the Cr environment in MIL-101 stays intact after integration with rGO. The C 1s spectrum (Figure 3c) can be decomposed into several components representing different carbon bonding environments. The primary peak at about 285.6 eV corresponds to C–C/C=C bonds found in the sp^2-hybridized carbon of the graphene lattice, indicating the presence of rGO sheets. Other components at around 285.9–287.1 eV are assigned to C–O functional groups, such as hydroxy or epoxy groups, while the peak near 287.7 eV can be attributed to O–C=O groups, originating from the carboxylate ligands of the terephthalate linkers in MIL-101 and residual oxygen functionalities on rGO [26]. The presence of these oxygen groups suggests that the reduction of graphene oxide is

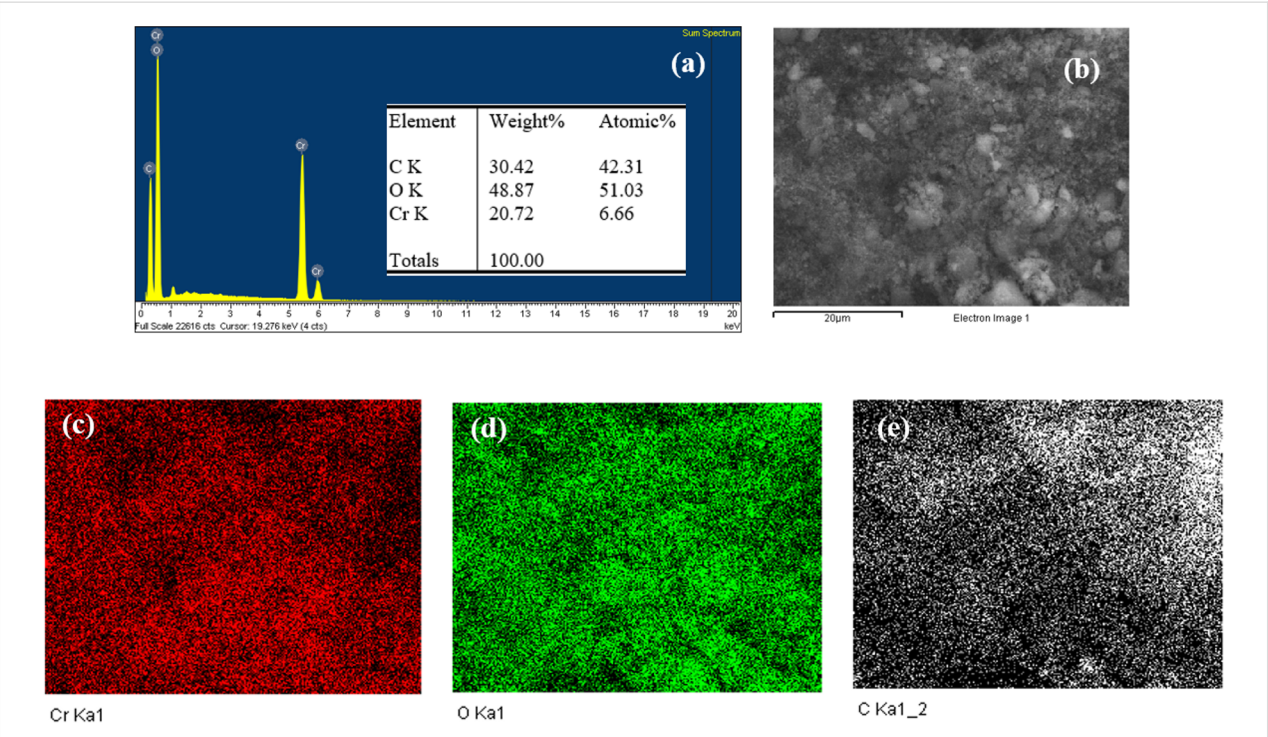

Figure 2: EDX elemental mapping and elemental composition of MIL-101/rGO (3.3), (a) EDX spectrum, (b) electron image, (c) chromium element mapping, (d) oxygen element mapping, and (e) carbon element mapping.

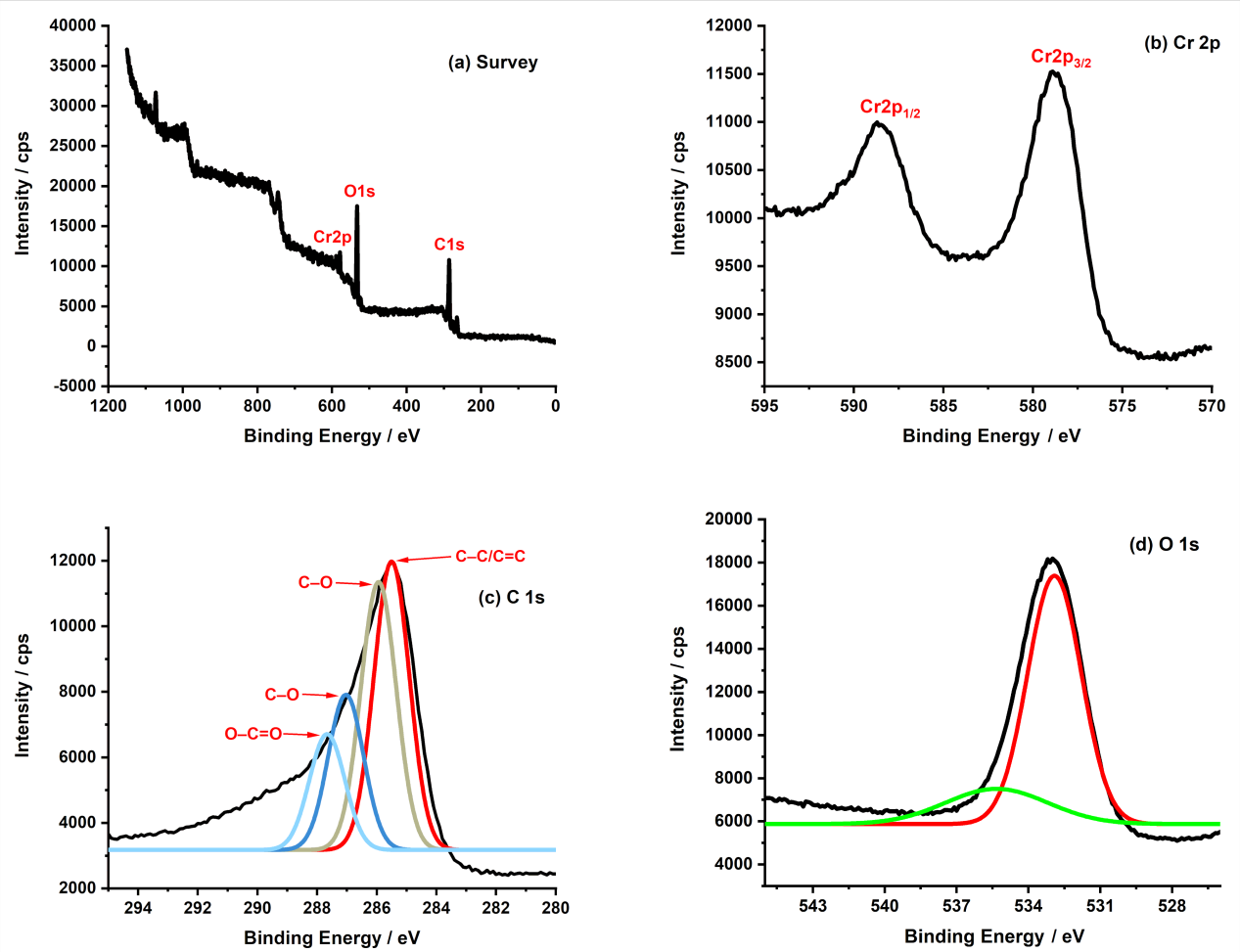

Figure 3: XPS spectra of the MIL-101/rGO (3.3): (a) survey spectrum, (b) high-resolution Cr 2p spectrum, (c) high-resolution C 1s spectrum, and (d) high-resolution O 1s spectrum.

partial and that surface functional groups remain, helping to facilitate interactions between rGO sheets and MIL-101 particles. The O 1s spectrum (Figure 3d) shows two main contributions. The peak around 532.9 eV is due to Cr–O bonds within the metal–oxo clusters of MIL-101(Cr), confirming the formation of the MOF framework. The second feature at approximately 535.8 eV can be attributed to oxygen species in C–O groups, hydroxy groups, or adsorbed water molecules associated with the rGO surface and the porous MOF structure [27]. The presence of these oxygen-containing species further supports the coexistence of MIL-101 and rGO within the composite. Overall, the XPS results confirm the successful integration of MIL-101(Cr) and rGO, while preserving the Cr^{3+} oxidation state and the characteristic coordination environment of the MIL-101 framework.

The SEM images of rGO, MIL-101, and the MIL-101/rGO composite are shown in Figure 4. The rGO sample (Figure 4a) displays a typical wrinkled, sheet-like morphology that offers a large surface area and a conductive substrate for material deposition. The pristine MIL-101 (Figure 4b) consists of irregular polyhedral particles that tend to aggregate, forming relatively compact clusters. In contrast, the MIL-101/rGO composite (Figure 4c) reveals that MIL-101 particles are dispersed on the wrinkled rGO sheets. The rGO sheets serve as a supporting scaffold, helping to separate the MIL-101 particles and reduce their aggregation to some extent. This structural characteristic benefits the dispersion of the MOF particles and enhances electron transfer within the composite material.

Electrochemical determination of ciprofloxacin (CPR) at MIL-101/rGO/GCE

Electrochemical behavior of CPR

Figure 5a compares the cyclic voltammograms of CPR recorded at different electrodes in 0.1 M BR buffer (pH 4) (see Supporting Information File 1, Figure S2). A weak and poorly defined oxidation peak is observed at the bare GCE, indicating sluggish electron-transfer kinetics. Upon modification with

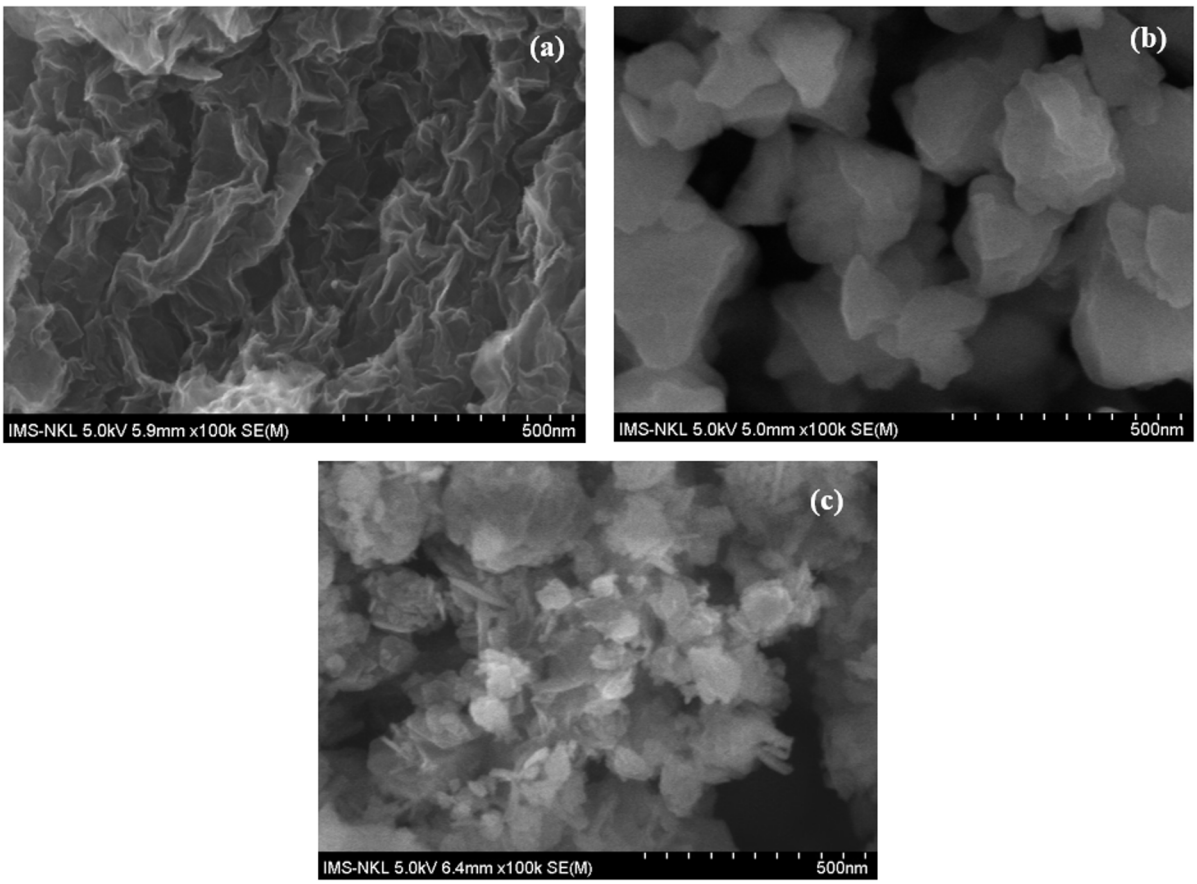

Figure 4: SEM observation of (a) rGO, (b) MIL-101, and (c) MIL-101(Cr)/rGO (3.3).

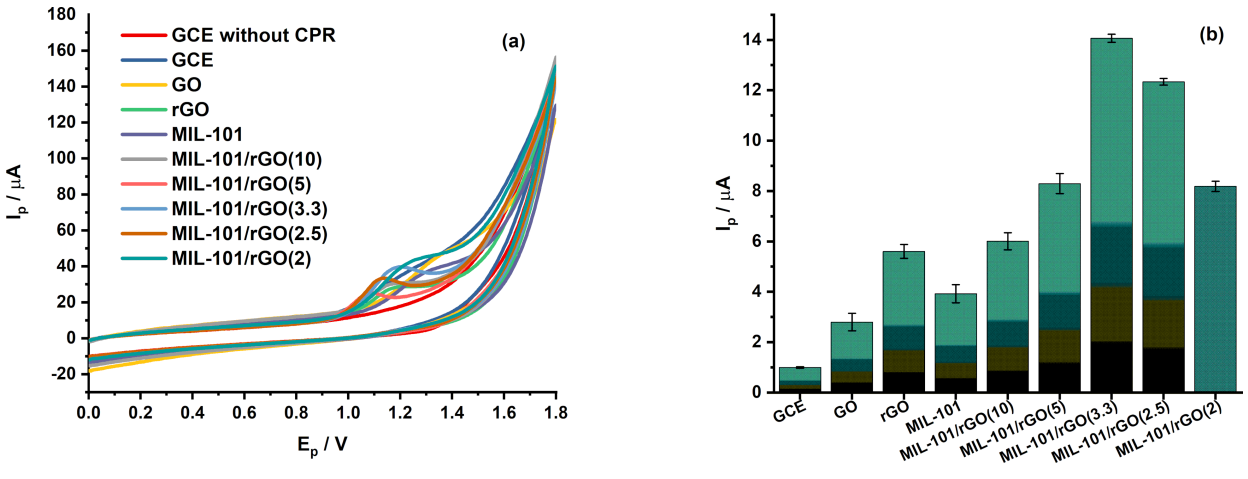

Figure 5: (a) Cyclic voltammograms (CVs) recorded at different electrodes in 0.1 M BRS buffer (pH 4) containing 15 µM CPR at a scan rate of 0.1 V/s and (b) comparison of the corresponding peak currents obtained at various electrodes (n = 3).

MIL-101 or rGO, the anodic peak current increases noticeably, reflecting improved adsorption and conductivity. The obtained peak potentials (E_p) for GCE, GO/GCE, rGO/GCE, MIL-101/GCE, MIL-101/rGO(10)/GCE, MIL-101/rGO(5)/GCE, MIL-101/rGO(3.3)/GCE, MIL-101/rGO(2.5)/GCE, and MIL-101/rGO(2)/GCE were 1.203, 1.150, 1.166, 1.288, 1.153, 1.072, 1.175, 1.125, and 1.219 V, respectively. In general, after modification of the electrode surface with these materials, the oxida-

tion peak potential of CPR shifted to lower potentials compared with bare GCE (1.203 V), accompanied by a significant increase in peak current. This behavior indicates that the modified materials can effectively enhance the electrocatalytic activity toward CPR oxidation. Notably, the MIL-101/rGO composite electrodes exhibit a much higher oxidation response than either MIL-101/GCE or rGO/GCE alone, demonstrating an apparent synergistic effect between the high surface area and adsorption capability of MIL-101 and the excellent electrical conductivity of rGO. Among the investigated compositions, MIL-101/rGO(3.3)/GCE provides the highest and most reproducible peak current (Figure 5b), and was therefore selected for subsequent experiments.

Effect of pH

The impact of solution pH on the electrochemical oxidation of CPR was studied over a pH range of 2–9 (Figure 6). The oxidation peak current rises with pH up to 4, then gradually declines at higher pH levels, showing that both CPR's protonation state and its interaction with the electrode significantly influence the electrochemical response (Supporting Information File 1, Figure S3). As a result, pH 4 was selected as the optimal condition. Additionally, the oxidation peak potential shifts linearly toward less positive values as pH increases. The linear relationship between peak potential and pH indicates that protons participate in the electrode process.

$$E_{\mathrm{CPR}} = (1.4790 \pm 0.0241) + (-0.0663 \pm 0.0041)\,\mathrm{pH};$$
$$r^2 = 0.9778$$

The slope of approximately 0.066 V·pH^{-1} is close to the theoretical Nernstian value, indicating that the number of transferred electrons is similar to that of protons. This result suggests a proton-coupled electron-transfer mechanism for CPR oxidation.

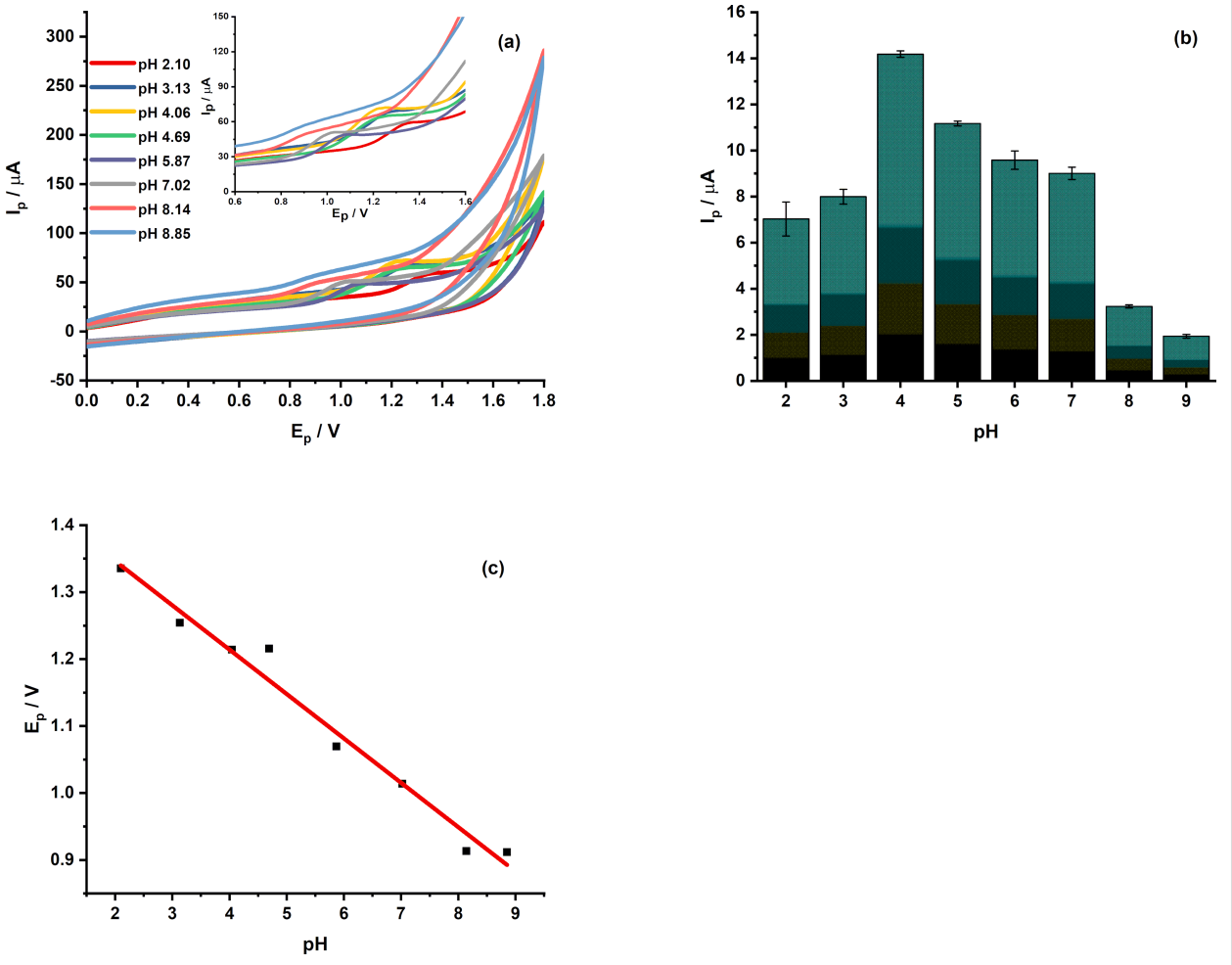

Figure 6: (a) CVs of MIL-101/rGO(3.3)/GCE recorded in 0.1 M BR buffer over the pH range of 2–9 containing 15 µM CPR at a scan rate of 0.1 V·s^{-1} and the inset shows the magnified view of the peak potential region, (b) variation of the oxidation peak current with pH, and (c) dependence of the oxidation peak potential on pH.

Effect of scan rate and kinetic analysis

The effect of scan rate on the electrochemical response of CPR at MIL-101/rGO(3.3)/GCE was examined over the range of 0.05–0.40 $V \cdot s^{-1}$ (Figure 7). The oxidation peak current increases linearly with the square root of the scan rate (Figure 7a), indicating that CPR oxidation is mainly controlled by diffusion [28].

$$I_{CPR} = (-0.7720 \pm 0.4714) + (26.1564 \pm 1.0341) v^{1/2};$$
$$r^2 = 0.9892$$

Furthermore, based on Laviron's theory [29], the linear dependence of peak potential on the natural logarithm of scan rate confirms the irreversible nature of the oxidation process (Figure 7c).

$$E_{CPR} = (1.1274 \pm 0.0024) + (0.0321 \pm 0.0013) \ln v;$$
$$r^2 = 0.9895$$

For an irreversible electrochemical system, the charge-transfer coefficient (α) was assumed to be 0.5, as is common in the literature [30].

From the slope of the E_{CPR}–ln v plot, the product of α and the number of transferred electrons (n) was calculated to be 0.7999, leading to an estimated n value of approximately 1.6. Although this does not correspond to an integer, it reasonably indicates the involvement of two electrons in the oxidation process. When combined with the pH-dependent study, the results further suggest that the electrochemical oxidation of CPR at the modified electrode likely involves a two-electron, two-proton transfer process, aligning with previously reported electrochemical oxidation mechanisms of CPR [31]. The proposed oxidation pathway of CPR is schematically illustrated in Scheme 1.

Optimization of DPV parameters

To achieve maximum sensitivity, the parameters for differential pulse voltammetry (DPV) were systematically optimized. The accumulation potential, accumulation time, pulse ampli-

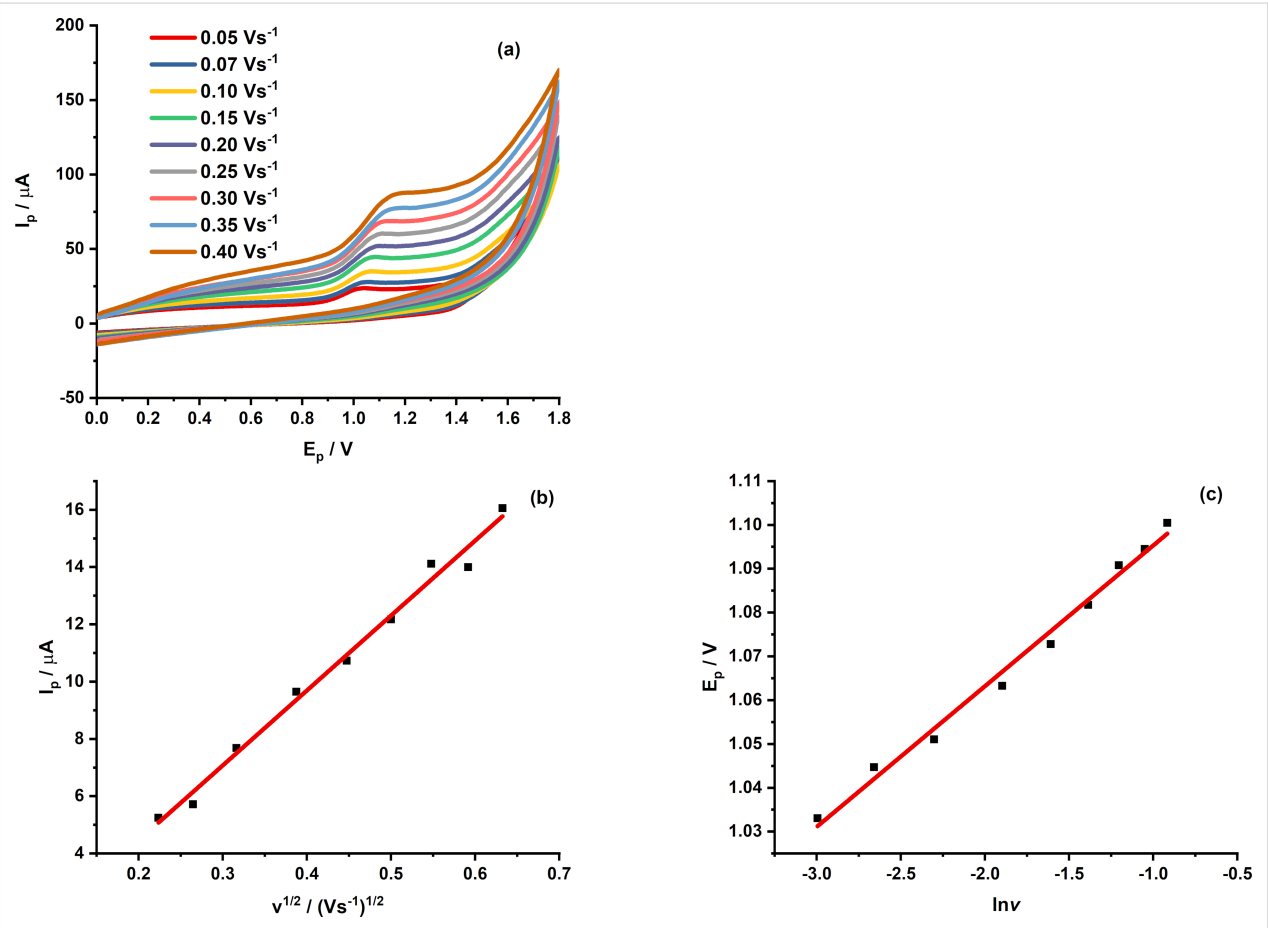

Figure 7: (a) Cyclic voltammograms of MIL-101/rGO(3.3)/GCE recorded in 0.1 M BR buffer (pH 4) containing 15 µM ciprofloxacin at scan rates from 0.05 to 0.40 $V \cdot s^{-1}$; (b) linear relationship between the peak current and the square root of scan rate ($v^{1/2}$), and (c) linear dependence of the peak potential of ciprofloxacin on the natural logarithm of scan rate (ln v).

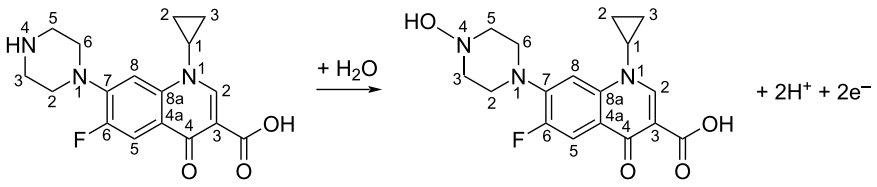

Scheme 1: The oxidation mechanism of CPR at MIL-101/rGO/CGE.

tude, and potential step were investigated individually (Supporting Information File 1, Figure S4–S7). The optimal conditions were determined to be an accumulation potential of 0 V, an accumulation time of 4 s, a pulse amplitude of 0.11 V, and a voltage step of 0.010 V. Under these conditions, the oxidation peak current of CPR reached its maximum while maintaining a good peak shape and stable signal.

Analytical performance and linear range

The analytical performance of the proposed sensor was evaluated by recording the DPV responses at increasing analyte concentrations (Figure 8a). As the CPR concentration rose, the peak current steadily increased, indicating that the electrochemical signal highly depends on the CPR concentration. The calibration plot of peak current versus concentration is shown in Figure 8b. Two linear regions are observed within the concentration ranges of 0.25–9.41 and 9.41–24.39 μM.

The corresponding regression equations are described as follows

$$\text{Range 1}: 0.25-9.41\,\mu\text{M},$$
$$I_{\text{CPR}} = (0.7790 \pm 0.0226) + (0.7109 \pm 0.0049) C_{\text{CPR}};$$
$$r^2 = 0.9990$$

$$\text{Range 2}: 9.41-24.39\,\mu\text{M},$$
$$I_{\text{CPR}} = (3.3577 \pm 0.0747) + (0.4247 \pm 0.0045) C_{\text{CPR}};$$
$$r^2 = 0.9992$$

The presence of two linear ranges indicates a change in the interaction between the CPR molecules and the electrode surface at higher concentrations. At lower concentrations, CPR molecules are effectively adsorbed onto the active sites of the MIL-101/rGO-modified electrode, resulting in higher sensitivity. However, as the concentration increases, the number of available active sites gradually decreases due to partial surface occupation by CPR molecules. As a result, the slope of the calibration curve decreases slightly in the higher-concentration range. This behavior shows the beginning saturation of active sites on the electrode surface, which is common in adsorption-controlled electrochemical sensing systems. However, a strong linear relationship is still maintained across a wide concentration range, demonstrating the good analytical performance of the proposed sensor for quantitative analysis.

The limit of detection (LOD_{CPR}) and the limit of quantification (LOQ_{CPR}) were 0.11 and 0.36 μM, respectively. Table 2 shows the LOD and linear range of the proposed DPV and compares them with published reports. The LOD of the proposed sensor

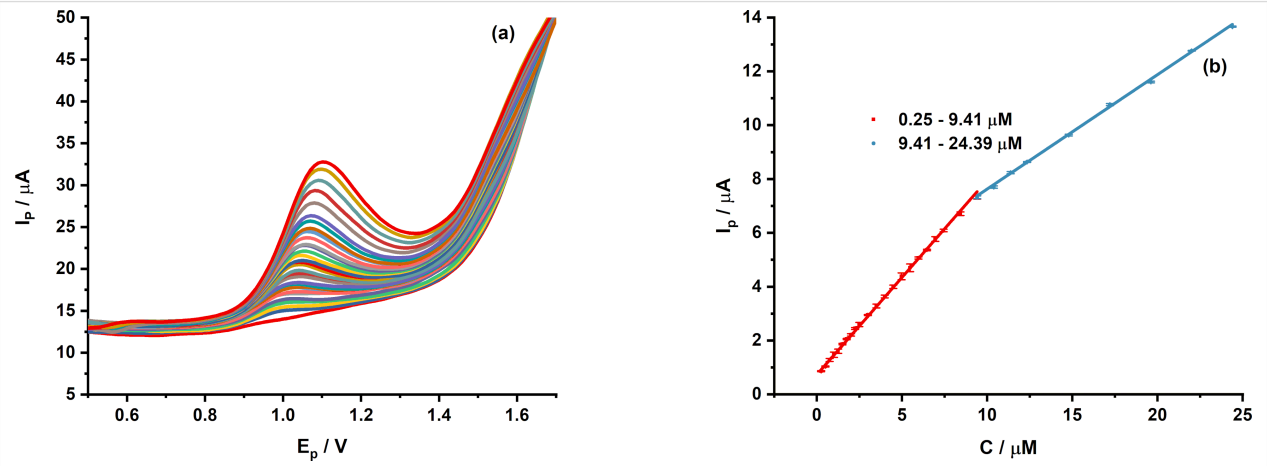

Figure 8: (a) DPV curves of MIL-101/rGO(3.3)/GCE recorded in 0.1 M BRS buffer (pH 4) at CPR concentrations ranging from 0.25 to 24.39 μM and (b) corresponding calibration plots of peak current versus ciprofloxacin concentration.

Table 2: Comparison of the analytical performance of the proposed MIL-101/rGO/GCE with previously reported electrochemical sensors for CPR determination.

Electrodes	Methods	Linear range (μM)	LOD (μM)	Real samples	Ref.
CB–PLA (3D-printed) sensor	–	1.0–12.5	0.3	tap water and synthetic urine	[32]
Poly [Mn(Chr)$_3$]Cl$_2$/PGE	SWV	1–200	0.536	pharmaceutical and urine samples	[33]
AgNPs-CB-Ch/GCE	SWV	3.1–24.8; 36.9–130.3	0.48	synthetic urine samples	[34]
GaTCPP(Ni)-Nafion/SPCE	DPV	200–1000	118	pharmaceutical samples	[35]
MWCNT/GCE	chronoamperometric	40–1000	6	urine and serum samples	[36]
CNSs/GCE	DPV	0.5–5.0	0.15	water sample and medicinal formulations	[37]
{[Co(HL)(bix)]·H$_2$O}$_n$/GCE	DPV	2–20	0.135	water samples	[38]
[Co(HL)(bimb)·H$_2$O]}$_n$/GCE	DPV	1–14	0.082	water samples	[38]
MIL-101/rGO/GCE	DPV	0.25–9.41	0.110	pharmaceutical formulations	this study

was comparable to previous sensors. The advantage of using the MIL-101(Cr)/rGO composite comes from the synergistic combination of its two components. MIL-101(Cr) has a high surface area and abundant porous structure, providing numerous active sites and strong adsorption capability for the target molecules; rGO offers high electrical conductivity, facilitating rapid electron transfer.

Repeatability, reproducibility, and stability

The measurement repeatability of the proposed sensor was evaluated at different CPR concentrations (1.0, 2.5, 5.0, 10.4, and 24.4 μM). Differential pulse voltammetry (DPV) responses were recorded over ten consecutive measurements, and the relative standard deviation (RSD) values were calculated and compared with half of the Horwitz RSD. The obtained RSD values were significantly lower than half of the Horwitz RSD, indicating excellent repeatability and analytical precision of the sensor (Figure 9a).

The reproducibility of the sensor was further assessed using independently prepared MIL-101/rGO-modified electrodes fabricated under identical conditions (Figure 9b). The peak current response was measured as I_{CPR} = 4.29 ± 0.16 μA, corresponding to an RSD of 3.70%. The low RSD value (<5%) confirms the good fabrication reproducibility of the proposed electrode.

The long-term stability of the sensor was evaluated using a single electrode stored in BR buffer at low temperature after use

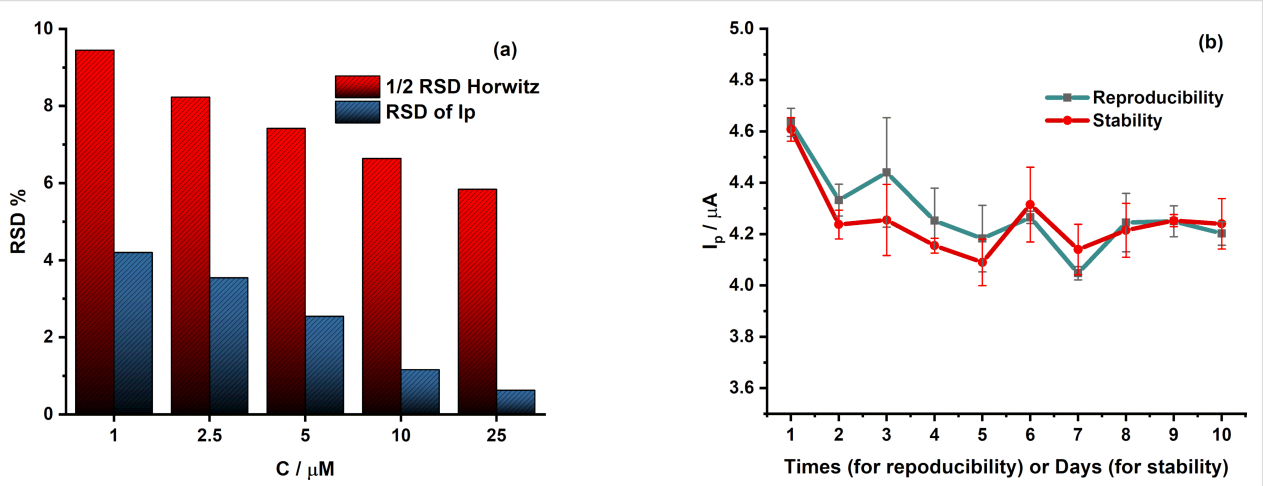

Figure 9: (a) Relative standard deviation of the anodic peak currents obtained from DPV measurements recorded over ten consecutive scans at the MIL-101/rGO(3.3)/GCE in 0.1 M B-R buffer (pH 4) containing CPR at different concentrations (1.0, 2.5, 5.0, 10.4, and 24.4 μM), in comparison with half of the Horwitz RSD (1/2 RSD$_H$) and (b) reproducibility and long-term stability of the MIL-101/rGO(3.3)/GCE evaluated from the peak current response toward ciprofloxacin (5.0 μM) in 0.1 M Britton–Robinson buffer (pH 4), including ten repeated measurements using independently prepared electrodes and the current response recorded over ten days.

and tested over several days (Figure 9b). The peak current was recalled as I_{CPR} = 4.25 ± 0.14 μA with an RSD of 3.33%. After ten days of storage, approximately 92% of the initial current response was retained. The low RSD values together with the high current retention demonstrate the satisfactory long-term stability and reliable performance of the MIL-101/rGO-modified electrode.

Interference study

The selectivity of the proposed sensor toward ciprofloxacin (CPR) was evaluated in the presence of common inorganic ions and organic compounds, including $CaCl_2$ (denoted as C1), NaCl (C2), K_2SO_4 (C3), $Al(NO_3)_3$ (C4), $Mg_3(C_6H_5O_7)_2$ (C5), NH_4Cl (C6), citric acid (C7), saccharine (C8), D-sorbitol (C9), ascorbic acid (C10), D-glucose (C11), and lactose (C12). An interfering species was considered to have a significant effect on the CPR peak current when the absolute relative deviation exceeded 5%.

As shown in Figure 10, no significant interference was observed for most of the tested species, even when their concentrations were more than 100-fold higher than that of CPR. These results demonstrate that the proposed sensor possesses good selectivity and strong anti-interference capability, making it suitable for the determination of CPR in complex sample matrices.

Application to pharmaceutical samples

The proposed DPV method was used to determine CPR in various commercial pharmaceutical formulations using the standard addition method (Table 3). The recovery values obtained ranged from 95.91% to 104.67%, demonstrating good accuracy of the method. The slightly higher recovery for Tablets 2 (104.67%) may be due to excipients in the formulation. Some excipients can produce weak electrochemical responses or contribute to background currents near CPR oxidation potentials, which can slightly raise the measured peak current and cause a minor overestimation of the analyte concentration. However, these recoveries are within the acceptable range for pharmaceutical analysis (90–110%), confirming the reliability of the developed DPV method for analyzing CPR in real samples.

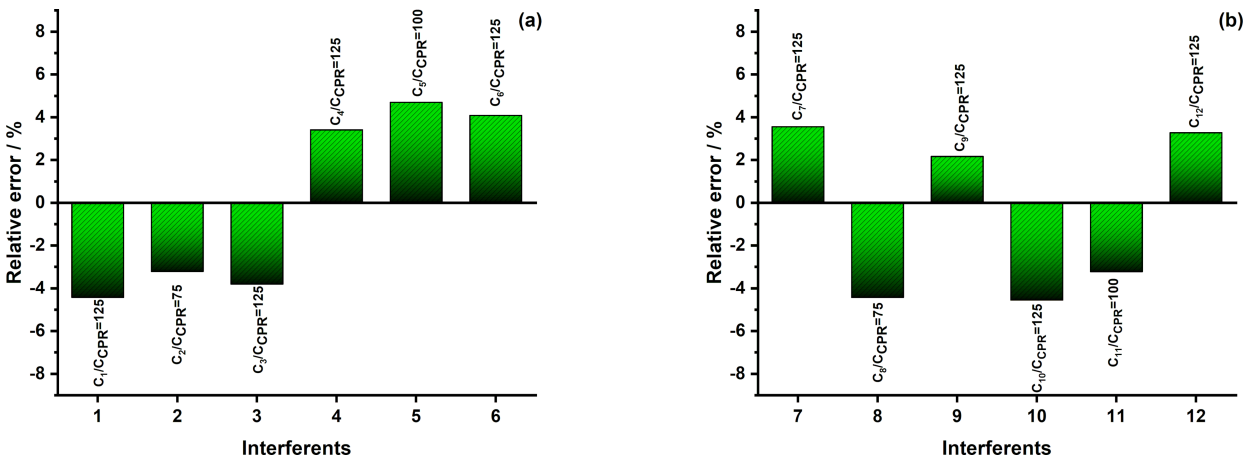

Figure 10: Relative error (RE%) caused by the interference of selected inorganic (a) and organic (b) species at different concentration ratios.

Table 3: Determination and recovery of CPR in commercial pharmaceutical formulations by DPV at MIL-101/rGO(3.3)/GCE.[a]

Notation	CPR content ± SD (μM)[b]	CPR content ± SD (mg)[c]	Spiked (μM)	Found ± SD (μM)[b]	Recovery (%)
Tablets 1 (Label 500 mg CPR/unit)	1.4376 ± 0.0182	479.3 ± 3.0	1.0	2.4089 ± 0.0299	97.13
Tablets 2 (Label 500 mg CPR/unit)	1.5656 ± 0.0281	512.1 ± 7.9	1.0	2.6123 ± 0.0158	104.67
Powder of oral suspension (Label 250 mg CPR/unit)	1.4851 ± 0.0172	245.6 ± 3.9	1.0	2.4442 ± 0.0257	95.91

[a]SD: standard deviation of three repeated measurements; [b]CPR concentration calculated in electrochemical cell; [c]CPR amount calculated in one unit of drug by DPV method.

Conclusion

In this work, an electrochemical sensor based on a MIL-101/reduced graphene oxide (MIL-101/rGO) modified glassy carbon electrode was successfully developed for detecting ciprofloxacin. MIL-101/rGO, synthesized using a simple ultrasonic-assisted method, displayed a favorable microstructure and strong interfacial interaction between MIL-101 and rGO, leading to an improved electrochemical response to ciprofloxacin oxidation. Electrochemical investigations showed that the modified electrode exhibited enhanced electrochemical performance and increased catalytic activity toward CPR oxidation compared to the bare electrode. Under optimal experimental conditions, the proposed sensor demonstrated a broad linear response range with a low detection limit, along with good selectivity against common interfering substances. Additionally, the sensor exhibited excellent repeatability, strong reproducibility in fabrication, and reliable long-term stability. The practical application of the method was confirmed through successful detection of CPR in pharmaceutical products with acceptable recoveries. Overall, the MIL-101/rGO-modified electrode is a reliable and efficient electrochemical sensing platform for CPR detection and shows potential for routine pharmaceutical analysis and related electrochemical sensing research.

Supporting Information

Supporting Information File 1

Additional figures.
[https://www.beilstein-journals.org/bjnano/content/supplementary/2190-4286-17-35-S1.pdf]

Funding

Hue University partially funded this research under the Core Research Program No. NCTB.DHH.2025.05.

Author Contributions

Nguyen Quang Man: conceptualization; funding acquisition; writing – original draft; writing – review & editing. Nguyen Ngoc Nghia: conceptualization; funding acquisition; writing – original draft; writing – review & editing. Nguyen Vinh Phu: investigation; methodology; resources; validation; visualization. Vo Thi Khanh Ly: investigation; methodology; resources; validation; visualization. Le Lam Son: investigation; methodology; resources; validation; visualization. Pham Khac Lieu: investigation; methodology; resources; validation; visualization. Le Thi Hong Phong: investigation; methodology; validation; visualization. Nguyen Dinh Luyen: supervision. Dinh Quang Khieu: writing – review & editing.

ORCID® iDs

Nguyen Quang Man - https://orcid.org/0000-0001-6511-1236
Nguyen Ngoc Nghia - https://orcid.org/0009-0009-9166-7815
Nguyen Vinh Phu - https://orcid.org/0000-0003-2389-3422
Vo Thi Khanh Ly - https://orcid.org/0009-0005-0854-3290
Le Lam Son - https://orcid.org/0000-0002-8693-7472
Pham Khac Lieu - https://orcid.org/0000-0002-9002-1416
Le Thi Hong Phong - https://orcid.org/0000-0001-8825-6243
Nguyen Dinh Luyen - https://orcid.org/0009-0004-3926-9282
Dinh Quang Khieu - https://orcid.org/0000-0003-3473-6377

Data Availability Statement

All data that supports the findings of this study is available in the published article and/or the supporting information of this article.

References

1. Thai, T.; Salisbury, B. H.; Zito, P. M. *Ciprofloxacin;* StatPearls Publishing LLC, 2025.
2. Peñafiel, M. E.; Vanegas, E.; Bermejo, D.; Matesanz, J. M.; Ormad, M. P. *Hyperfine Interact.* **2019,** *240,* 71. doi:10.1007/s10751-019-1612-9
3. Al-howri, B. M.; Ismail, S.; Khajavian, M. *Environ. Monit. Assess.* **2025,** *197,* 1095. doi:10.1007/s10661-025-14454-z
4. Thakur, R.; Singh, A.; Dhanwar, R.; Kadam, S.; Waghmare, U.; Lodha, T.; Lopes, B. S.; Prakash, O. *Discov. Sustain.* **2025,** *6,* 232. doi:10.1007/s43621-025-01048-5
5. Wang, J.; Li, X.; Xu, Z.; Xu, L. *Food Sci. Hum. Wellness* **2025**. doi:10.26599/fshw.2025.9250607
6. Ahmadi, K.; Nasirimoghadam, S.; Mohammadjafar, F.; Hashemi, S. F.; Zeeb, M. *Anal. Lett.* **2026,** *59,* 935–948. doi:10.1080/00032719.2025.2519463
7. Elgendy, K.; Zaky, M.; Alaa Eldin, T.; Fadel, S. *Results Chem.* **2023,** *5,* 100749. doi:10.1016/j.rechem.2022.100749
8. de Vroom, S. L.; Pistorius, M. C. M.; Bijleveld, Y. A.; Geerlings, S. E.; Mathôt, R. A. A.; van Hest, R. M.; Jager, N. G. L. *Ther. Drug Monit.* **2022,** *44,* 552–557. doi:10.1097/ftd.0000000000000969
9. Qiu, S.; Wang, Y.; Wan, J.; Han, J.; Ma, Y.; Wang, S. *Appl. Surf. Sci.* **2020,** *525,* 146511. doi:10.1016/j.apsusc.2020.146511
10. Zorainy, M. Y.; Gar Alalm, M.; Kaliaguine, S.; Boffito, D. C. *J. Mater. Chem. A* **2021,** *9,* 22159–22217. doi:10.1039/d1ta06238g
11. Keshta, B. E.; Yu, H.; Wang, L.; Yi, H.; Jian, S.; Uddin, M. A.; Ouyang, C.; Wang, Y.; Yuan, X.; Zhang, Y.; Jin, Y.; Basit, A.; Owais Malik, M.; Awan, K. M. *npj Clean Water* **2025,** *8,* 15. doi:10.1038/s41545-024-00413-7
12. Öztekin, D.; Arbağ, H.; Yaşyerli, S. *Arabian J. Sci. Eng.* **2025,** *50,* 9905–9918. doi:10.1007/s13369-024-09915-5
13. Mustafa, Z.; Kumar, D.; Swain, B. P.; Pradhan, B. B.; Ghadai, R. K. *Sci. Rep.* **2026,** *16,* 536. doi:10.1038/s41598-025-29897-0
14. Wang, S.; Zou, H.-J.; Sun, J.; Lu, C.; Gao, X.; Han, X. *J. Sol-Gel Sci. Technol.* **2025,** *116,* 2717–2732. doi:10.1007/s10971-025-06994-0
15. Jilani, A.; Dustgeer, M. R.; Ansari, M. O.; Zaka, A.; Mansoor, M. A.; Melaibari, A. A.; Ibrahim, H. *J. Water Process Eng.* **2025,** *80,* 109086. doi:10.1016/j.jwpe.2025.109086
16. Gu, J.; Yin, X.; Bo, X.; Guo, L. *ChemElectroChem* **2018,** *5,* 2893–2901. doi:10.1002/celc.201800588

17. Wu, Y.; Luo, H.; Wang, H.; Wang, C.; Zhang, J.; Zhang, Z. *J. Colloid Interface Sci.* **2013,** *394,* 183–191. doi:10.1016/j.jcis.2012.11.049
18. Wu, Y.; Luo, H.; Zhang, L. *Environ. Sci. Pollut. Res.* **2015,** *22,* 17238–17243. doi:10.1007/s11356-015-5364-z
19. Miller, J. N.; Miller, J. C.; Miller, R. D. *Statistics and Chemometrics for Analytical Chemistry,* 7th ed.; Pearson, 2005.
20. Yasin, G.; Arif, M.; Shakeel, M.; Dun, Y.; Zuo, Y.; Khan, W. Q.; Tang, Y.; Khan, A.; Nadeem, M. *Adv. Eng. Mater.* **2018,** *20,* 1701166. doi:10.1002/adem.201701166
21. Jiao, X.; Qiu, Y.; Zhang, L.; Zhang, X. *RSC Adv.* **2017,** *7,* 52337–52344. doi:10.1039/c7ra10809e
22. Ferey, G.; Mellot-Draznieks, C.; Serre, C.; Millange, F.; Dutour, J.; Surble, S.; Margiolaki, I. *Science* **2005,** *309,* 2040–2042. doi:10.1126/science.1116275
23. Wei, G.; Yu, J.; Gu, M.; Tang, T. B. *J. Appl. Phys.* **2016,** *119,* 224102. doi:10.1063/1.4953357
24. Meneses-Ruiz, E.; Escobar, J.; Mora, R. J.; Montoya, J. A.; Barrera, M. C.; Solís-Casados, D.; Escobar-Alarcón, L.; Del Ángel, P.; Laredo, G. *Oil Gas Sci. Technol.* **2021,** *76,* 56. doi:10.2516/ogst/2021038
25. Huang, X.; Hu, Q.; Gao, L.; Hao, Q.; Wang, P.; Qin, D. *RSC Adv.* **2018,** *8,* 27623–27630. doi:10.1039/c8ra04789h
26. Jiang, J.; Zhu, L.; Chen, H.; Sun, Y.; Qian, W.; Lin, H.; Han, S. *J. Mater. Sci.* **2019,** *54,* 1422–1433. doi:10.1007/s10853-018-2913-0
27. Vo, T. K.; Kim, J.-H.; Kwon, H. T.; Kim, J. *J. Ind. Eng. Chem. (Amsterdam, Neth.)* **2019,** *80,* 345–351. doi:10.1016/j.jiec.2019.08.013
28. Bard, A. J.; Faulkner, L. R. *Russ. J. Electrochem.* **2002,** *38,* 1364–1365. doi:10.1023/a:1021637209564
29. Laviron, E. *J. Electroanal. Chem. Interfacial Electrochem.* **1979,** *101,* 19–28. doi:10.1016/s0022-0728(79)80075-3
30. Li, C. *Colloids Surf., B* **2007,** *55,* 77–83. doi:10.1016/j.colsurfb.2006.11.009
31. Tajik, S.; Beitollahi, H.; Zaeimbashi, R.; Sheikhshoaei, M.; Askari, M. B.; Salarizadeh, P. *J. Mater. Sci.: Mater. Electron.* **2021,** *32,* 17558–17567. doi:10.1007/s10854-021-06288-5
32. Henriques, B. F.; Neumann, A.; Bertolim, L. V.; de Freitas, R. C.; Silva, L. R. G.; Stefano, J. S.; Janegitz, B. C. *Electroanalysis* **2025,** *37,* e12008. doi:10.1002/elan.12008
33. Shitahun, A.; Atlabachew, M.; Aragaw, B. A.; Benor, A.; Metto, M.; Abebe, A. *Int. J. Electrochem. Sci.* **2025,** *20,* 100937. doi:10.1016/j.ijoes.2025.100937
34. Meireles, L. M.; Silva, R. M.; da Silva, R. C.; Okumura, L. L.; Moreira, R. P. L.; Silva, T. A. *J. Solid State Electrochem.* **2025,** *29,* 3111–3122. doi:10.1007/s10008-024-06033-y
35. Shepa, J.; Király, N.; Demeterová, J.; Shepa, I.; Hviščová, P.; Volavka, D.; Kožár, M.; Šišoláková, I.; Oriňaková, R.; Zeleňák, V.; Almáši, M. *Microchem. J.* **2025,** *218,* 115638. doi:10.1016/j.microc.2025.115638
36. Fotouhi, L.; Alahyari, M. *Colloids Surf., B* **2010,** *81,* 110–114. doi:10.1016/j.colsurfb.2010.06.030
37. Ipte, P. R.; Kumar, S.; Satpati, A. K. *J. Environ. Sci. Health, Part A: Toxic/Hazard. Subst. Environ. Eng.* **2020,** *55,* 142–150. doi:10.1080/10934529.2019.1674591
38. Xiang, R.; Qin, T.; Liu, Y.; Lan, L.; Dong, X.; Srivastava, D.; Parvez, M. K.; Al-Dosari, M. S.; Kumar, A.; Pan, Y. *Microchem. J.* **2025,** *209,* 112594. doi:10.1016/j.microc.2024.112594

License and Terms

BEILSTEIN JOURNAL OF NANOTECHNOLOGY

Interface-engineered Caco-2 cell culture on a collagen-coated liquid–liquid interface in a microfluidic device

Satoru Kuriu* and Soo Hyeon Kim*

Full Research Paper

Open Access

Address:
Institute of Industrial Science, The University of Tokyo, 4-6-1 Komaba, Meguro-ku, Tokyo 153-8505 JAPAN

Email:
Satoru Kuriu* - kurius@iis.u-tokyo.ac.jp;
Soo Hyeon Kim* - shkim@iis.u-tokyo.ac.jp

* Corresponding author

Keywords:
Caco-2; collagen; FC-43; gut-on-a-chip; liquid–liquid interface

Beilstein J. Nanotechnol. **2026,** *17,* 760–768.
https://doi.org/10.3762/bjnano.17.53

Received: 10 March 2026
Accepted: 26 May 2026
Published: 11 June 2026

This article is part of the thematic issue "Nanotechnology for cross-scale analysis: comprehensive evaluation of water environments".

Guest Editors: Y. Sasaki and T. Minami.

Abstract

Epithelial tissues form selective barriers essential for physiological homeostasis. Conventional in vitro models rely on solid substrates, which limit the physicochemical flexibility of the cellular microenvironment. Here, we introduce a microfluidic platform in which a collagen-coated liquid–liquid interface formed between perfluorocarbon (FC-43) and culture medium serves as a substrate for epithelial cell adhesion. By culturing Caco-2 cells in the device, we show that the liquid interface supports cell attachment and the formation of monolayers. Immunofluorescence observation reveals the development of tight junctions and organized actin cytoskeletons, indicating early-stage epithelial maturation. Our new microfluidic system enables the formation of stable liquid–liquid interfaces that serve as viable and flexible substrates for epithelial cell culture, offering new opportunities for multiphase microfluidic models of epithelial barriers.

Introduction

Epithelial tissues form selective barriers that regulate the transport of molecules, ions, and gases; they play an important role in physiological homeostasis [1]. In vitro models of epithelial barriers, particularly culturing Caco-2 cells, have been widely used to study the function of the epithelial tissues [2-4]. The microfluidic culture system known as gut-on-a-chip enables the cultivation of Caco-2 cells under conditions that more closely recapitulate the in vivo intestinal environment. By precisely controlling fluid flow and inducing mechanical stimuli, this platform provides physiologically relevant mechanical cues that are difficult to reproduce in conventional static culture systems [5-7]. Gut-on-a-chip platforms recapitulate the apical-basolateral compartmentalization of the human intestinal epithelium by dividing upper and lower microchannels with a solid porous

membrane, upon which intestinal epithelial cells are cultured to establish a polarized epithelial barrier. Although porous membranes enable compartmentalization, they may also impose non-physiological diffusion barriers and mechanical constraints.

Liquid–liquid interfaces provide a mechanically soft and dynamically reconfigurable environment that more closely mimics native cellular microenvironments than rigid solid substrates. Unlike conventional solid culture surfaces, liquid–liquid interfaces offer a distinct platform for cell culture, enabling a scaffold-free and mechanically tunable environment that eliminates the rigidity and pore-related constraints inherent to synthetic solid membranes [8-10]. Importantly, culturing cells at a liquid–liquid interface provides a unique opportunity to decouple biochemical signaling from substrate-imposed mechanical constraints, thereby enabling more physiologically relevant investigation of epithelial barrier formation, transport functions, and mechanobiological responses that are otherwise difficult to isolate in conventional solid-supported systems. Moreover, when functionalized with extracellular matrix proteins, such interfaces can support uniform epithelial maturation and stable monolayer formation, demonstrating their potential as engineered bioactive substrates [10]. Owing to their dynamic responsiveness to chemical and physical stimuli, such interfaces can also serve as reservoirs or delivery media for gases and hydrophobic molecules [11]. Incorporating a liquid–liquid interfacial strategy into microfluidic cell culture systems may therefore offer an alternative to porous membrane-based designs and mitigate the inherent limitations of synthetic solid membranes in gut-on-a-chip platforms. Among candidate materials, perfluorocarbon liquids such as FC-43 are particularly attractive due to their chemical inertness, immiscibility with aqueous media, and high gas solubility [11], making them well suited for multiphase microfluidic applications.

In this study, we propose a novel microfluidic cell culture system by utilizing a collagen-coated liquid–liquid interface that serves as a cell-adhesion substrate for epithelial cells (Figure 1A). The rectangular cuboid-shaped microfluidic device allows for stable formation of the liquid–liquid interface for cell culture by sequential flow manipulation (Figure 1B). Using Caco-2 cells, a well-known epithelial cell line, we demonstrate that cells can adhere and form monolayers on the liquid–liquid interface. Immunofluorescence images reveal the formation of tight junctions and organized actin cytoskeletons, indicating epithelial early-stage maturation. Our results establish liquid–liquid interfaces as viable and functional substrates for epithelial cell culture and highlight their potential for the development of flexible, multiphase microfluidic models of epithelial barrier.

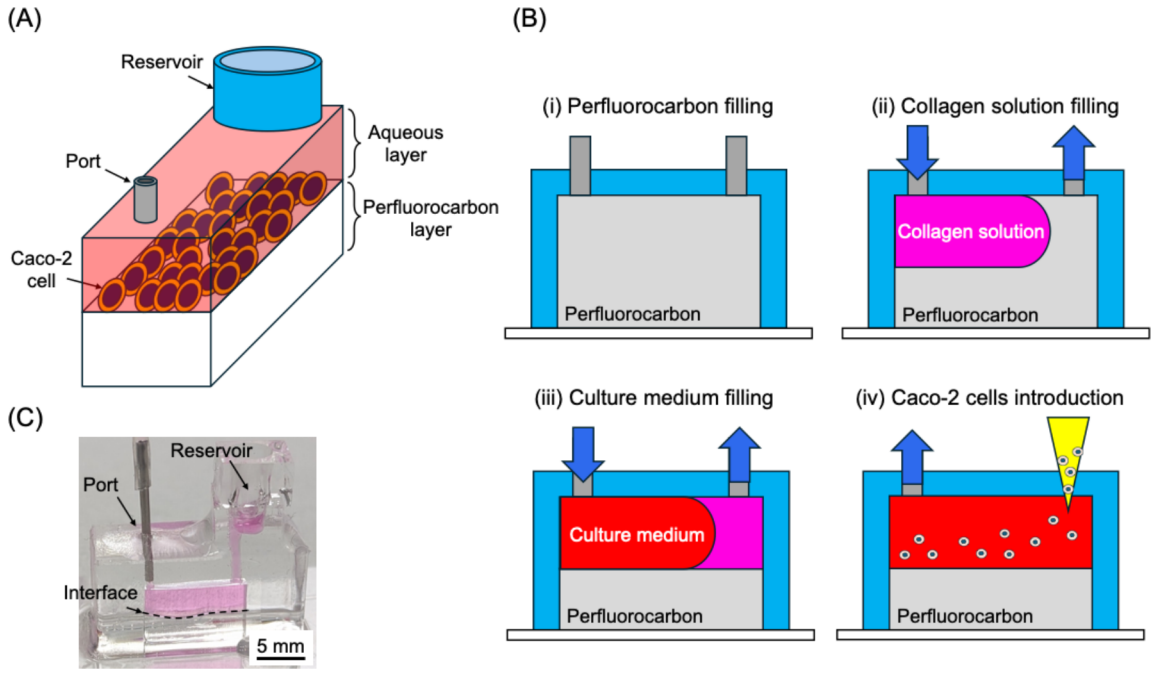

Figure 1: Illustration of the liquid–liquid interface formation. (A) Concept of the microfluidic device. (B) Fluid operation description: (i) FC-43 filling, (ii) collagen solution filling, (iii) culture medium filling, and (iv) Caco-2 cells introduction. (C) Fabricated microfluidic device. The dashed line indicates the boundary of the liquid–liquid interface.

Results and Discussion

Liquid–liquid interface formation in the microfluidic device

The liquid–liquid interface was formed by first filling the microchannel with the perfluorocarbon liquid FC-43, followed by the introduction of an aqueous solution containing collagen (Figure 1B-ii). The effect of channel dimensions on the formation of the liquid–liquid interface was evaluated using the rectangular cuboid-shaped microfluidic device.

First, channel height and length were fixed at 7 and 10 mm, respectively, while the channel width was varied (1.0, 1.5, 2.0, 5.0, and 10.0 mm). Liquid–liquid interfaces were subsequently formed in each channel by introducing collagen solution at 50 µL/min. Here, when forming the liquid–liquid interface, a meniscus develops. To quantify the extent of this meniscus, we introduced rectangularity as an easily interpretable indicator. Rectangularity is calculated using Equation 1 based on the collagen region observed on the channel height × channel length plane of the microfluidic device (i.e., 7 mm × 10 mm in this case, see Figure 2, Figure 3, and Supporting Information File 1, Figures S1–S3) and the minimum bounding rectangle of the collagen solution region.

$$\text{Rectangularity (\%)} = \frac{\text{The area of the collagen solution region}}{\text{The area of the minimum bounding rectangle of the collagen solution region}} \times 100 \quad (1)$$

The rectangularity for each channel size is shown in Figure 3. When the channel width ranged from 1 to 2 mm, the rectangularity of the aqueous layer was 94% or higher; however, when the channel width was 5 or 10 mm, the rectangularity decreased to 88% (Figure 3). These results suggest that channel width affects the formation of the liquid–liquid interface. To analyze this effect, the "Bond number" (B_o), a dimensionless parameter defined as

$$B_0 = \frac{\rho g L^2}{\sigma}, \quad (2)$$

was introduced to evaluate whether gravitational forces or interfacial tension dominate when two fluids of different densities are in contact. Here, ρ denotes the density difference between FC-43 and the collagen solution, g is the gravitational acceleration, L is the channel width, and σ is the interfacial tension coefficient. In this experiment, as the channel width L was varied, its effect on the Bond number was directly assessed. Taking the Bond number for a channel width of 1 mm as a reference, the Bond numbers for channel widths of 1.5, 2, 5, and 10 mm were 2.25, 4, 25, and 100 times greater, respectively. For channel widths of 5 and 10 mm, the Bond number increased by one to two orders of magnitude. As the Bond number increases, gravi-

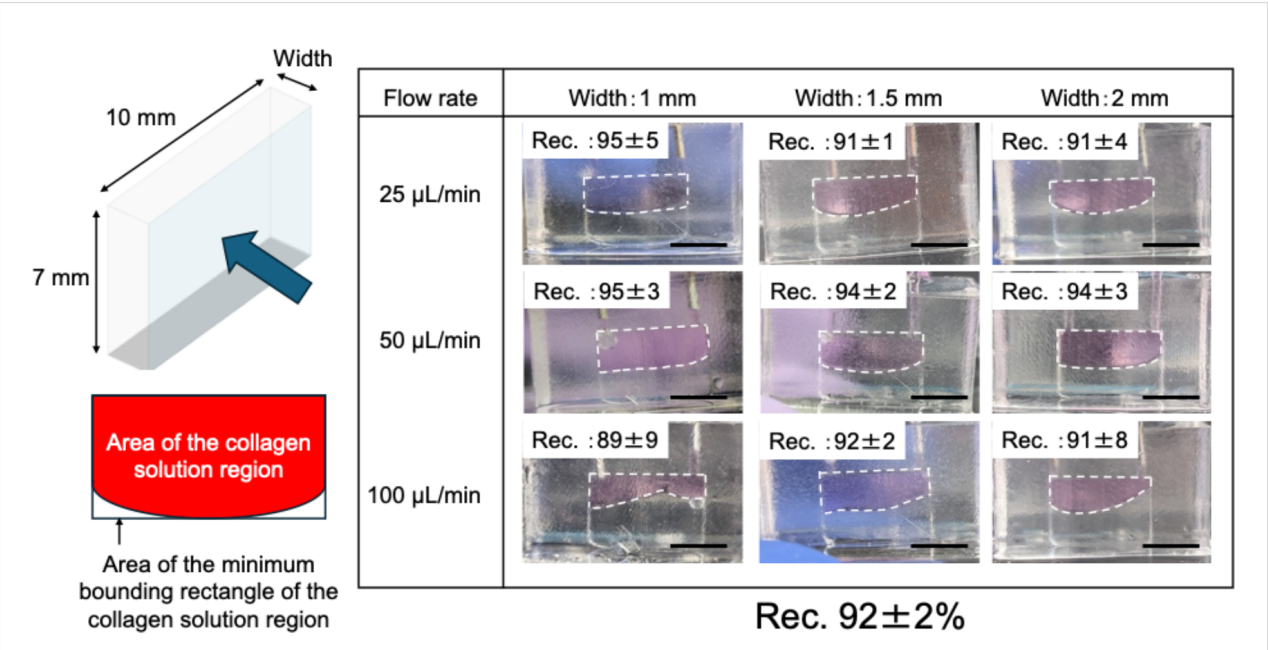

Figure 2: Rectangularity of the collagen solution region with respect to channel dimension (7 mm × 10 mm × width) and collagen solution introduction flow rate. The collagen region was imaged by a smartphone followed by the direction indicated by arrow. Rectangularity is abbreviated as "Rec".

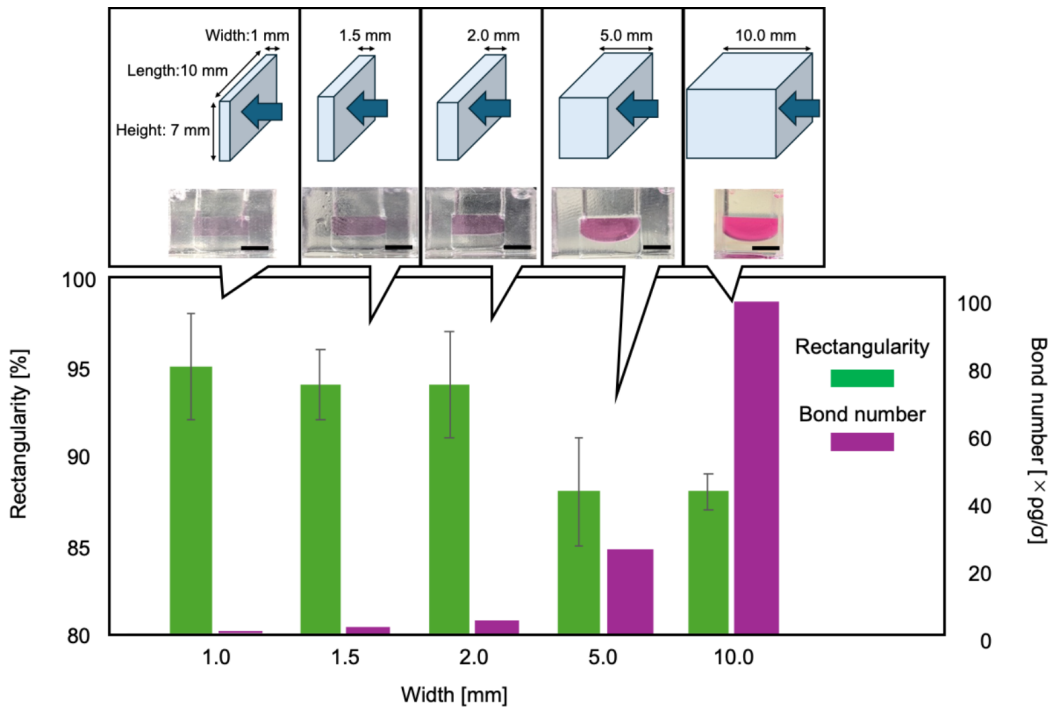

Figure 3: Rectangularity and Bond number as functions of the channel width (1.0, 1.5, 2.0, 5.0, and 10.0 mm). Representative interface images are shown above each bar. The images of the collagen solution region were captured from the direction indicated by the arrows. Scale bars are 5 mm. $n = 3$.

tational forces increasingly dominate over interfacial tension. Thus, for channel widths of 5 and 10 mm, the gravitational effect on the aqueous layer exceeds that of surface tension, resulting in a pronounced meniscus and a reduction in rectangularity. In this study, a high rectangularity was interpreted as indicating an interface nearly parallel to the channel bottom, which is favorable for microscopic observation; accordingly, devices exhibiting high rectangularity were selected for the demonstration. For a practical application, the device with a width of 2 mm was selected for the cell culture experiments because it offered advantages in operation, including easier bubble removal.

In addition, the effect of channel height on the formation of the liquid–liquid interface was evaluated (Figure 4). The channel height was varied at 7, 5, and 4 mm. When the height was 4 mm, the FC-43 layer was almost completely displaced upon the introduction of the collagen solution, preventing interface formation. At a height of 5 mm, the liquid–liquid interface was formed, but the rectangularity decreased to approximately 87%, comparable to the rectangularity observed for aqueous layers in channels 5 and 10 mm wide at a height of 7 mm. These results indicate that channel height is also a critical parameter for the formation of the liquid–liquid interface.

Rectangularity was evaluated by varying both the channel size and the flow rate of the collagen solution (Figure 2, Supporting Information File 1, Figures S1–S3). Our results suggest that interface formation is largely insensitive to the flow rate of the collagen solution, whereas the channel size significantly governs the interfacial shape.

Caco-2 cell culture on the liquid–liquid interface

The feasibility of adhesive cell culture on the liquid–liquid interface with a collagen layer was demonstrated by culturing Caco-2 cells (a human colorectal adenocarcinoma cell line). After forming the liquid–liquid interface using FC-43 and collagen-containing serum-free DMEM, the cell suspension was introduced and seeded at a density of 1.5×10^5 cells/cm^2. The growth of Caco-2 cells on the liquid–liquid interface is shown in Figure 5. The images were captured near the center of the channel. At two days post-seeding, most Caco-2 cells had adhered to the interface, resulting in the formation of a monolayer. This monolayer was maintained for seven days. In this study, Caco-2 cell monolayer culture was performed using three independent devices. As a result, confluency reached 95 ± 3% after seven days of culture. Here, the images of the left, center and right regions of the channel for each device were acquired

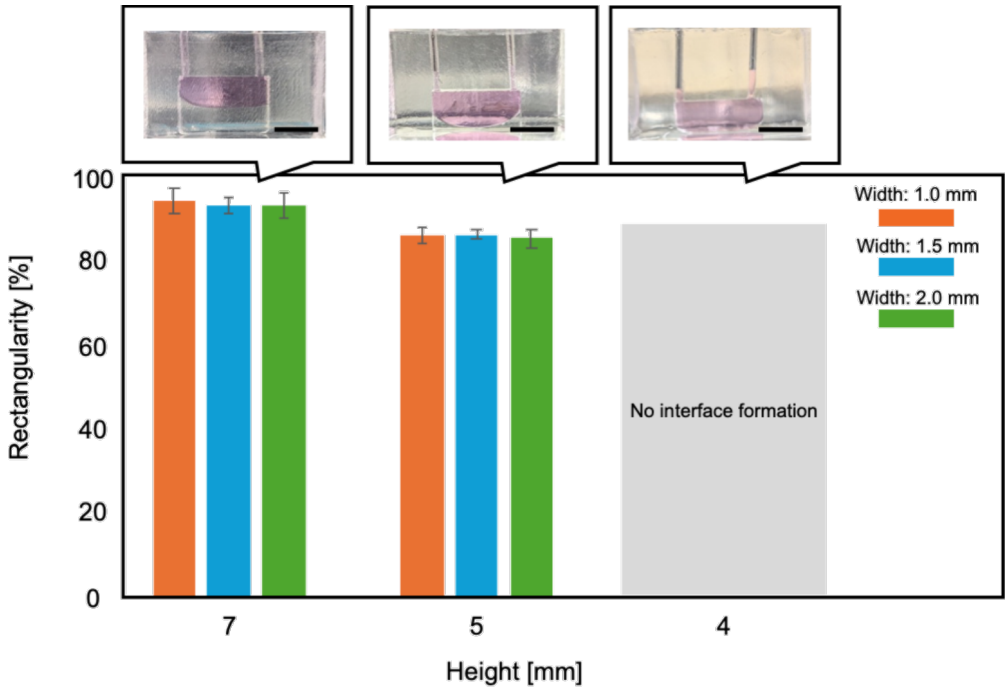

Figure 4: Rectangularity as a function of channel height (7, 5, and 4 mm). Representative interface images are shown above each bar. For a channel height of 4 mm, almost all of the FC-43 was replaced by the collagen solution; therefore, the rectangularity was not calculated, and it is labeled as "No interface formation". Scale bars are 5 mm. n = 3.

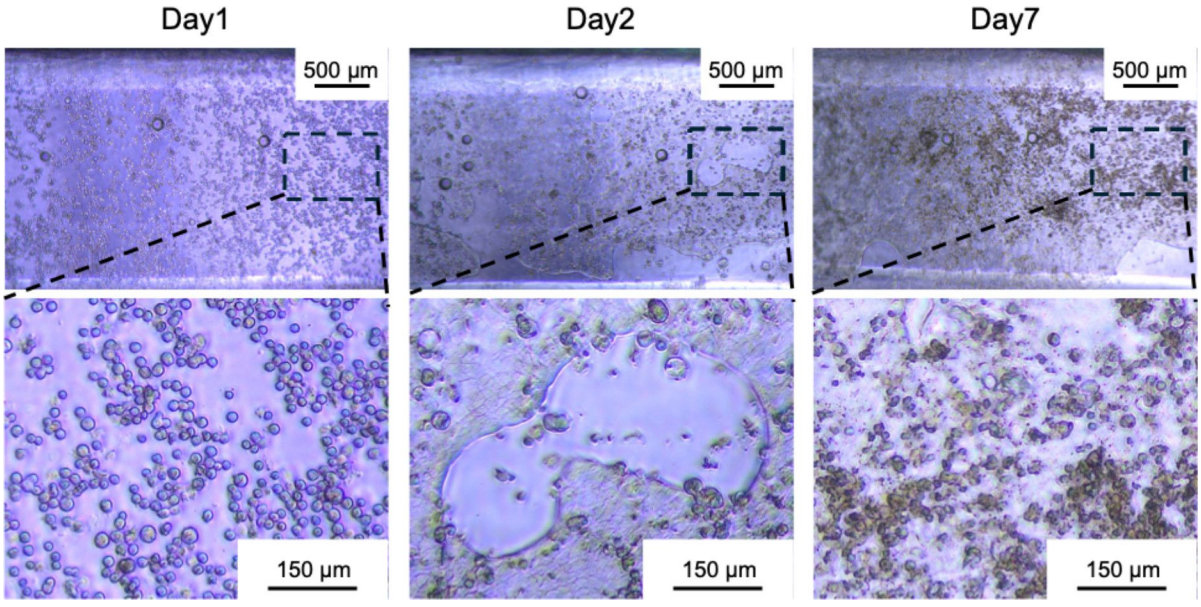

Figure 5: Time-lapse images of the progression of Caco-2 cells at the liquid–liquid interface. Images indicate Day1, Day2 and Day7, respectively. Region with a lower number of cells is magnified to show that Caco-2 cells grow on the interface.

on day seven of culture (see Supporting Information File 1, Figure S4), and confluency was calculated. Previous studies have suggested that Caco-2 cells begin to exhibit early functional characteristics of the intestinal epithelium, such as tight junction formation, after approximately seven days of culture [12]. In the present study, we therefore chose a period of seven

days of culture to assess the early-stage maturation of Caco-2 monolayers from a proof-of-concept perspective. Here, the liquid–liquid interface remained intact and was stably maintained throughout the cell culture period (data is not shown).

To observe whether collagen was coated on the liquid–liquid interface, immunostaining for collagen was performed (Supporting Information File 1, Figure S5). Compared to the device without collagen coating, fluorescence was observed in the collagen-coated device. In addition, to evaluate the effect of collagen coating on the liquid–liquid interface, the behavior of Caco-2 cells seeded onto a liquid–liquid interface without collagen coating is shown in Supporting Information File 1, Figure S6. Caco-2 cells did not adhere on the liquid–liquid interface to form a monolayer; instead, they aggregated and were observed floating on the liquid–liquid interface. Those results indicate that bringing the collagen solution into contact with FC-43 results in the formation of a collagen layer on the liquid–liquid interface that is sufficiently robust to support cell adhesion.

Caco-2 cells monolayer maturation

Immunofluorescence staining was performed to observe the characteristics of cultured Caco-2 cells as an intestinal epithelial model. Figure 6 shows a comparison of immunofluorescence images of ZO-1, F-actin, and nuclei in Caco-2 cells cultured in the microfluidic device and in 96-well plates. Under both conditions, epifluorescence imaging shows that the nuclei, ZO-1, and F-actin signals are localized within the same focal plane and are distributed across the entire liquid–liquid interface formed in the microfluidic device, indicating the formation of a monolayer. Although autofluorescence from FC-43 was observed in the images of the microfluidic devices, ZO-1 localization at cell–cell junctions was confirmed, suggesting the formation of epithelial barrier properties in Caco-2 cells cultured in the microfluidic device [13,14]. F-actin localization was observed under both conditions, suggesting that the cytoskeletal organization supporting the epithelial structure was maintained in Caco-2 cells cultured in the microfluidic device. Colocalization of ZO-1 with F-actin at cell–cell borders indicates the formation of mature tight junctions and the establishment of a functional epithelial barrier. Taken together, these results suggest that Caco-2 cells [15,16] cultured in the microfluidic

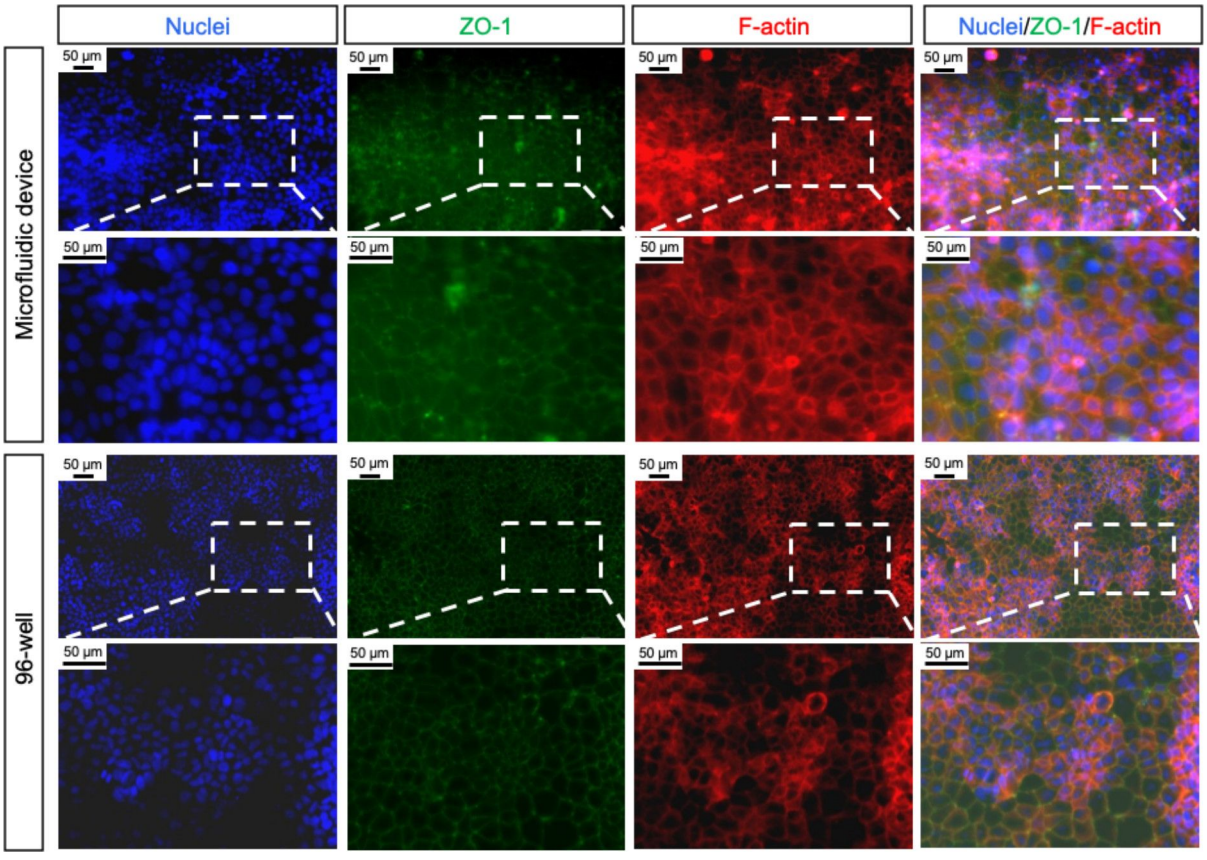

Figure 6: Immunofluorescence images of Caco-2 cells cultured in a microfluidic device and 96-well plates. Nuclei, ZO-1, F-actin and Merge images are displayed.

device formed an epithelial monolayer with tight junctions and supporting cytoskeletal organization, recapitulating intestinal epithelial characteristics. Caco-2 cell culture and immunostaining within the microfluidic device were conducted in triplicate (n = 3), and representative results are shown in this study.

Conclusion

We propose a unique rectangular cuboid-shaped microfluidic device that enables Caco-2 cell culture on a liquid–liquid interface. The collagen-coated liquid–liquid interface was formed by sequentially perfusing collagen-containing aqueous solution into the microfluidic channel filled with perfluorocarbon FC-43. Caco-2 cells were successfully cultured on the interface by forming a monolayer, and immunofluorescence imaging confirmed tight-junction formation and organized actin cytoskeletons, indicating early-stage epithelial maturation. Unlike conventional systems that rely on plastic or silicone rubber substrates for cell adhesion, our system enables direct cell culture on a liquid–liquid interface, offering a novel platform with potential for advanced drug transport studies and co-culture experiments with other cell types. This approach is expected to open new avenues for functional assays, such as transepithelial electrical resistance or drug permeability studies and co-culture experiments with other cell types.

Experimental

Device materials, reagents, and Caco-2 cells

The materials for device fabrication and assembly were obtained from the following suppliers: PDMS (Silpot 184W/C, Dow Corning Toray, Tokyo, Japan) and cover glass (MICRO COVER GLASS, MATSUNAMI GLASS IND., LTD., Osaka, Japan). Reagents for experiments were obtained from the following suppliers: formaldehyde (FA) (Formaldehyde, FUJIFILM Wako Pure Chemical Corporation, Osaka, Japan), Triton X-100 (Triton^{TM}X-100, Sigma-Aldrich, St. Louis, MO, USA), ZO-1 antibody (ZO-1 Monoclonal Antibody [ZO1-1A12], Alexa Fluor^{TM} 488, Thermo Fisher Scientific Inc., Waltham, MA, USA), phalloidin (Phalloidin, Red Fluorescent Dye Conjugate, Acti-stain 555, Cytoskeleton, Inc., CO, USA), Hoechst33342 (Hoecst 33342 solution, Dojindo Laboratories, Kumamoto, Japan), PBS (D-PBS(−) (10×), Nacalai Tesque, Inc., Kyoto, Japan), DMEM (DMEM(1×)+GlutaMAX^{TM}-I, Gibco, Thermo Fisher Scientific Inc., Waltham, MA, USA), FBS (Fetal Bovine Serum, Gibco, Thermo Fisher Scientific Inc., Waltham, MA, USA), Collagen type I-C (Cellmatrix® Type I-C, Nitta Gelatin Inc., Osaka, Japan) and FC-43 (3M, St. Paul, MN, USA).

Device fabrication

The microfluidic device was fabricated by following soft lithography. The polyacetal plate was milled to fabricate the molds, which were designed by three-dimensional computer-aided design software. The fabrication process is shown in Supporting Information File 1, Figure S7. Briefly, PDMS was cast on molds and cured at 85 °C for 5 h (Figure S7i). The cured PDMS was removed from the mold and holes with diameters of 1.0 and 1.5 mm were punched for port and reservoir, respectively (Figure S7ii). Port and reservoir were attached on to the microfluidic device (Figure S7iii). A thin layer of uncured PDMS was applied to the bottom of the device, attached to a coverslip and cured at 85 °C for 2 h (Figure S7iv).

Caco-2 cell culture

The procedure of the Caco-2 cell culture in the microfluidic device is shown in Figure S8. First, the device was filled with FC-43 (Figure S8i). Next, collagen-containing serum-free DMEM (60 μg/mL) was introduced into the channel at a flow rate of 50 μL/min using a syringe pump (KDS, kd Scientific, MA, USA) from the port (Figure S8ii). In this study, the collagen concentration was selected as the optimal condition based on preliminary experiments (data not shown). In brief, excessively low collagen concentrations impede cell adhesion, while excessively high concentrations lead to gelation, making fluid handling impossible. The microfluidic device was put in the refrigerator (4 °C, 2 h) (Figure S8iii). Thereafter, culture medium was introduced into the channel at a flow rate of 10 μL/min for 10 min to replace the existing liquid layer (Figure S8iv). The human large intestinal cancer cell line Caco-2 cells (CACO-2, KAC Co., Ltd., Kyoto, Japan) were harvested and resuspended in culture medium (DMEM/FBS = 9:1) (Figure S8v). A portion of the cell suspension was aspirated using a pipette, and the pipette tip was mounted onto the device reservoir. The cell suspension was then introduced into the channel from the port using a syringe pump at a flow rate of 20 μL/min for 1 min, and Caco-2 cells were seeded onto the liquid–liquid interface at a density of 1.5×10^5 cells/cm^2. The microfluidic device was then put in an incubator (37 °C, 5% CO_2). The culture medium was replaced daily by flowing fresh medium through the channel at a flow rate of 10 μL/min for 10 min. For control experiments, Caco-2 cells were seeded into 96-well plates at a density of 1.5×10^5 cells/cm^2, and the culture medium was replaced daily. The microfluidic device and the 96-well plate were put in an incubator (37 °C, 5% CO_2).

Immunostaining procedure

For immunostaining, Caco-2 cells cultured in the channel device and 96-well plates for seven days were fixed with 4% FA/PBS for 20 min, followed by permeabilization with 0.5% Triton X-100/PBS at room temperature for 20 min (Supporting Information File 1, Figure S9ii,iv). Blocking was performed with 1% BSA/PBS at 4 °C overnight (Figure S9vi). The samples were then incubated at room temperature for 3 h in a solu-

tion containing ZO-1 antibody (5 μg/mL), phalloidin (0.1 μM), and Hoechst33342 (2 μg/mL). Between each procedure, PBS was filled to wash the channel or wells (Figure S9i,iii,v,vii).

For immunostaining, the collagen layer coated on the liquid–liquid interface was fixed with 4% FA/PBS for 20 min at room temperature for 20 min (Figure S10v). Blocking was performed with 1% BSA/PBS at 4 °C overnight (Figure S10vii). The samples were then incubated at room temperature for 3 h in a solution containing collagen antibody (5 μg/mL) (Figure S10ix). In the negative control experiment without collagen coating, the procedure was carried out in the same manner, except for the step shown in Figure S10ii.

Image acquisition and quantification

The appearance of the aqueous layer was captured using a smartphone (Google Pixel 9a, Google LLC, CA, USA). Bright-field images of the cells were acquired using an inverted microscope (Leica DMil, Leica Microsystems, Wetzlar, Germany) equipped with a FLEXACAM camera. Fluorescence images were acquired using an all-in-one fluorescence microscope (BZ-X700, Keyence Corporation, Osaka, Japan). The fluorescence images were saved in 14-bit TiFF format, and the images were processed using the ImageJ software (NIH).

Supporting Information

Supporting Information File 1

Additional figures.
[https://www.beilstein-journals.org/bjnano/content/supplementary/2190-4286-17-53-S1.pdf]

Funding

This work was supported by JSPS KAKENHI Grant Number JP23H03865, JP24K03302.

Author Contributions

Satoru Kuriu: conceptualization; data curation; formal analysis; investigation; methodology; validation; visualization; writing – original draft; writing – review & editing. Soo Hyeon Kim: funding acquisition; project administration; supervision; writing – review & editing.

ORCID® iDs

Satoru Kuriu - https://orcid.org/0000-0001-9328-4134

Data Availability Statement

All data that supports the findings of this study is available in the published article and/or the supporting information of this article.

Preprint

A non-peer-reviewed version of this article has been previously published as a preprint: https://doi.org/10.3762/bxiv.2026.10.v1

References

1. Zihni, C.; Mills, C.; Matter, K.; Balda, M. S. *Nat. Rev. Mol. Cell Biol.* **2016,** *17,* 564–580. doi:10.1038/nrm.2016.80
2. Wang, X.; Li, L.; Zhang, G. *RSC Adv.* **2019,** *9,* 34607–34616. doi:10.1039/c9ra06222j
3. Yokoi, F.; Deguchi, S.; Takayama, K. *Regener. Ther.* **2025,** *29,* 541–550. doi:10.1016/j.reth.2025.04.023
4. Xian, C.; Zhang, J.; Zhao, S.; Li, X.-G. *J. Tissue Eng.* **2023,** *14,* 20417314221149882. doi:10.1177/20417314221149882
5. Kim, H. J.; Huh, D.; Hamilton, G.; Ingber, D. E. *Lab Chip* **2012,** *12,* 2165–2174. doi:10.1039/c2lc40074j
6. Valiei, A.; Aminian-Dehkordi, J.; Mofrad, M. R. K. *APL Bioeng.* **2023,** *7,* 011502. doi:10.1063/5.0126541
7. Donkers, J. M.; van der Vaart, J. I.; van de Steeg, E. *Biomimetics* **2023,** *8,* 226. doi:10.3390/biomimetics8020226
8. Jia, X.; Minami, K.; Uto, K.; Chang, A. C.; Hill, J. P.; Ueki, T.; Nakanishi, J.; Ariga, K. *Small* **2019,** *15,* 1804640. doi:10.1002/smll.201804640
9. Ueki, T.; Uto, K.; Yamamoto, S.; Tamate, R.; Kamiyama, Y.; Jia, X.; Noguchi, H.; Minami, K.; Ariga, K.; Wang, H.; Nakanishi, J. *Adv. Mater. (Weinheim, Ger.)* **2024,** *36,* 2310105. doi:10.1002/adma.202310105
10. Sonoi, R.; Kamihira, M. *Sci. Rep.* **2024,** *14,* 12314. doi:10.1038/s41598-024-63115-7
11. Ariga, K. *Small* **2024,** *20,* 2305636. doi:10.1002/smll.202305636
12. Valenzano, M. C.; DiGuilio, K.; Mercado, J.; Teter, M.; To, J.; Ferraro, B.; Mixson, B.; Manley, I.; Baker, V.; Moore, B. A.; Wertheimer, J.; Mullin, J. M. *PLoS One* **2015,** *10,* e0133926. doi:10.1371/journal.pone.0133926
13. Ross, A. M.; Walsh, D. R.; Cahalane, R. M.; Marcar, L.; Mulvihill, J. J. E. *Biochem. Biophys. Rep.* **2021,** *27,* 101096. doi:10.1016/j.bbrep.2021.101096
14. Putt, K. K.; Pei, R.; White, H. M.; Bolling, B. W. *Food Funct.* **2017,** *8,* 406–414. doi:10.1039/c6fo01592a
15. Mazzei, A.; Pagliara, P.; Del Vecchio, G.; Giampetruzzi, L.; Croce, F.; Schiavone, R.; Verri, T.; Barca, A. *Biology (Basel, Switz.)* **2022,** *12,* 36. doi:10.3390/biology12010036
16. Nakajima, T.; Sasaki, K.; Yamamori, A.; Sakurai, K.; Miyata, K.; Watanabe, T.; Matsunaga, Y. T. *Biomater. Sci.* **2020,** *8,* 5615–5627. doi:10.1039/d0bm00763c

BEILSTEIN JOURNAL OF NANOTECHNOLOGY

Cross-scale design of chemosensor arrays: from molecular self-assembly in water to paper-based devices for metal ion detection

Yui Sasaki[1,2] and Tsuyoshi Minami[*3]

Perspective

Open Access

Address:
[1]Research Center for Advanced Science and Technology, The University of Tokyo, 4-6-1, Komaba, Meguro-ku, Tokyo 153-8904, Japan, [2]JST PRESTO, 4-1-8 Honcho, Kawaguchi, Saitama 332-0012, Japan, and [3]Institute of Industrial Science, The University of Tokyo, 4-6-1 Komaba, Meguro-ku, Tokyo 153-8505, Japan

Email:
Tsuyoshi Minami[*] - tminami@g.ecc.u-tokyo.ac.jp

* Corresponding author

Keywords:
chemosensor; metal ion; paper device; pattern recognition; self-assembly

Beilstein J. Nanotechnol. **2026,** *17,* 828–838.
https://doi.org/10.3762/bjnano.17.59

Received: 19 March 2026
Accepted: 22 May 2026
Published: 24 June 2026

This article is part of the thematic issue "Nanotechnology for cross-scale analysis: comprehensive evaluation of water environments".

Associate Editor: S. A. Claridge

Abstract

Monitoring metal ions in aquatic environments is essential for understanding ecosystem dynamics and assessing water quality. Chemosensors have emerged as powerful analytical tools at the molecular level that transduce ion-recognition events into optical signals. In particular, coordination with metal ions enables cross-reactive sensing, allowing for simultaneous detection of multiple analytes based on pattern recognition. This perspective summarizes advances in self-assembled chemosensor systems for metal ion detection and further developments to solid-state chemosensor array devices based on nanotechnologies. In practical chemosensor designs, dynamic covalent bonds between catechol and phenylboronic acid derivatives have been employed to provide a versatile strategy for the spontaneous preparation of chemosensor elements without extensive synthetic effort. Furthermore, integration of these self-assembled chemosensors into paper substrates enables portable detection platforms for on-site analysis without using stationary laboratory instruments. This cross-scale design strategy provides a promising approach for simultaneous detection of metal ions in various water environments across microscopic and macroscopic scales.

Introduction

Metal ions are essential species in biological systems; however, heavy metal ions act as pollutants and can damage organs and the immune system through the intake of contaminated food [1,2]. Globally, the monitoring of metal ion levels in water environments is significant.

Chemosensors are analytical tools at the molecular level that exhibit optical responses through colorimetric and fluorescence signals [3-5]; they have been widely applied to metal ion detection [6-11]. The detection principle of chemosensors relies on ion and molecular recognition chemistry [3]. Target metal ions

have various sizes and valencies; thus, simultaneous detection of multiple metal ions is desired [1,2]. In this regard, chemosensors provide multivalent interactions toward analytes, which allow the simultaneous detection of metal ions based on pattern recognition [12-16].

Chemosensor design relies on molecular-recognition chemistry, dye chemistry, and photochemistry [3]. Conventional chemosensors based on covalent bond chemistry require organic synthetic approaches in the chemosensor preparations [6-9]. Meanwhile, molecular self-assembly serves as a driving force for easy-to-obtain chemosensors through spontaneous preparation without a synthetic burden [17]. Moreover, the optical properties of chemosensors are tuned during association and dissociation upon analyte detection [18,19]. The performance of chemosensors has been widely evaluated in the solution state using conventional spectroscopic instruments [12-16], whereas the practical implementation of sensing systems remains challenging in on-site analysis [20,21]. Thus, the development of a solid-state chemosensor device is necessary for facile analyte detection.

To implement the cross-scale design concept, chemosensor elements should be highly dispersed on solid support materials possessing nanoarchitectures such as fiber structures. Paper substrates, which are commonly used in daily life, are eco-friendly and highly processable materials for disposable analytical devices [20-25]. In particular, the fiber structures of paper substrates provide unique functional nanoarchitectures [26,27]. Regarding analytical devices, such fiber-like nanostructures contribute to the homogeneous dispersion of chemosensor molecules through office printing technologies [28,29]. The printed chemosensor arrays on a paper substrate exhibit optical changes upon analyte capture, which are detected using portable recording apparatuses (e.g., smartphones, digital cameras, and flatbed scanners) [21,30]. Approaches using paper substrates as solid supports for chemosensor array devices enable on-site analysis without using stationary laboratory facilities.

Previous reviews have discussed chemosensors for metal ions [6-9], approaches for self-assembled chemosensors [17,19,31], chemosensor arrays (nanoparticles [32,33], polymers [34,35], and self-assembled elements [36]), solid-state analytical devices using gels [37,38] and paper substrates [21], and chemometric techniques [39] and their principles [40,41], independently. However, the conceptual connection between molecular-scale recognition events and device-level sensing architectures remains insufficiently explored. In this perspective, we propose a cross-scale design that bridges ion and molecular recognition chemistry with solid-state sensing devices incorporating nanoscale architectures for environmental monitoring of metal ions. This perspective introduces the principles of metal ion detection using chemosensors and the design strategy based on molecular self-assemblies for sensing multiple analytes based on pattern recognition [13,15]. After the discussion of the potential of self-assembled chemosensors and their arrays for simultaneous detection of metal ions in solution states, the concept is expanded to a paper-based chemosensor array device [20]. In this perspective, we introduce the new concept "cross-scale design", defined as an approach connecting molecular sensing in solution states and solid-state sensing, while maintaining or enhancing chemosensor behaviors compared with those in solution (Figure 1). In this context, the concept of cross-scale design refers to the hierarchical integration of

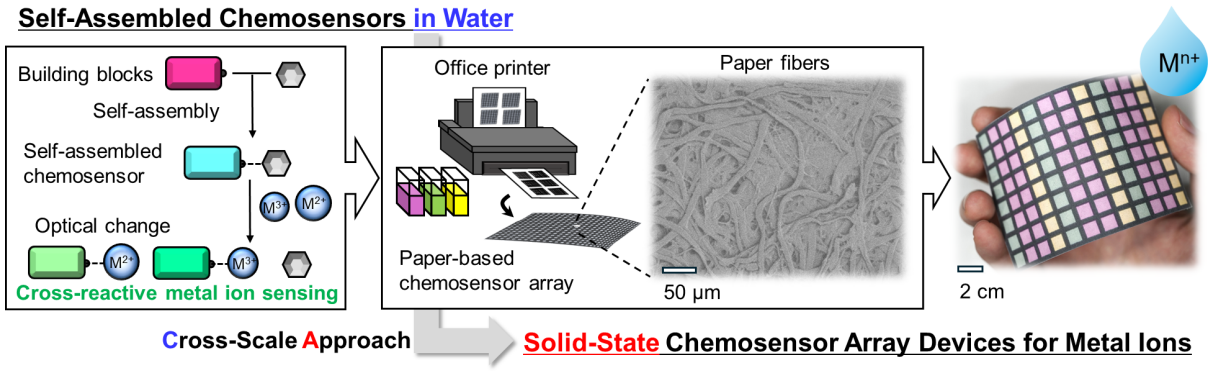

Figure 1: Conceptual figure showing this perspective on simultaneous metal ion detection based on self-assembled chemosensors and their devices through a cross-scale design. The middle panel of Figure 1 was adapted from [28] ("Nanoarchitectonics of highly dispersed polythiophene on paper for accurate quantitative detection of metal ions", © 2024 Y. Sasaki et al., published by the Royal Society of Chemistry, distributed under the terms of the Creative Commons Attribution 3.0 Unported License, https://creativecommons.org/licenses/by/3.0/). The rightmost panel of Figure 1 was adapted from [20] (© 2023 Y. Sasaki et al., distributed under the terms of the Creative Commons Attribution 4.0 International License, https://creativecommons.org/licenses/by/4.0).

sensing processes across multiple levels, from supramolecular chemosensors and pattern-recognition-based sensing to device-level architectures for practical environmental monitoring.

Discussion

Designs and preparation of chemosensors for the simultaneous detection of metal ions

As described in the Introduction, we aim to simultaneously discriminate multiple metal ions based on pattern recognition. In pattern recognition-driven chemical sensors, various response patterns including absorbance, fluorescence intensities, and wavelength changes are used as input data for pattern recognition [36]. To perform accurate analysis, appropriate designs of chemosensors are required. This section focuses on the design strategies based on molecular self-assemblies and the candidates for building blocks for chemosensor elements.

Categorization of chemosensor designs

In the simultaneous detection of multiple metal ions in aqueous media, chemosensors should satisfy the following requirements: They must exhibit different optical properties depending on the types of metal ions and their concentrations to obtain fingerprint-like response patterns, and they must be highly soluble [17]. Typical chemosensor molecules are covalently linked among the binding sites for analytes, optical units (chromophores and fluorophores), and manipulator units, if necessary (Figure 2A) [42]. To construct a chemosensor array, the variation of optical properties is significant, while the modification of chemosensor properties is limited by the synthetic effort required. Molecular self-assembly is a valid approach to spontaneously obtain an ensemble in aqueous media by mixing building blocks and to tune optical properties by changing the combination of building blocks [17,19,31].

One representative self-assembly-driven chemosensing system is an indicator-displacement assay (IDA) [31,43]. In this system, an indicator and a receptor unit spontaneously form a self-assembled chemosensor in aqueous media, accompanied by an optical change. Upon analyte addition, the indicator is released from the chemosensor ensemble, which induces optical recovery (Figure 2B). To further tune the optical properties of indicators, building blocks acting as optical manipulators are an appropriate strategy in self-assembled chemosensing. The chemosensor is formed using optical units (and the target binding site) and optical manipulators [13,15]. In contrast to the typical IDA, the approach using the optical unit serving as the target binding site and the optical manipulator induces distinct optical changes upon analyte capture (Figure 2C). This approach offers the advantage of facile preparation of chemosensors that display a variety of optical patterns, even with a small number of building blocks.

Selection of building blocks of chemosensors for metal ion sensing

The general strategy of metal-ion recognition primarily relies on multivalent coordination between target metal ions and donor atoms (e.g., nitrogen, oxygen, and sulfur) of binding sites [44]. Upon metal ion capture, the chemical information is visualized using optical units and further amplified by optical manipula-

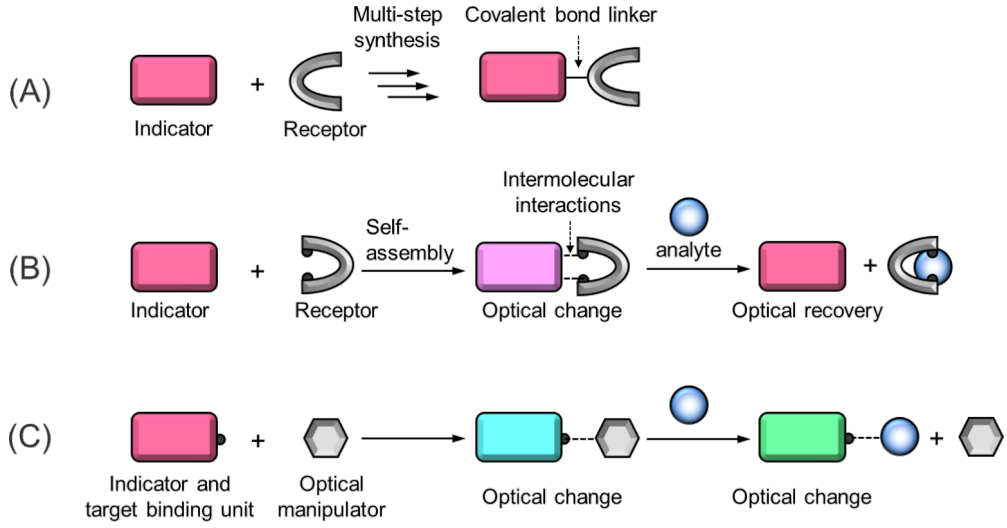

Figure 2: Categorization of chemosensor preparation and detection principles. (A) An indicator–spacer–receptor-based chemosensor based on covalent bond chemistry, (B) an indicator displacement assay for analyte capture based on a competitive reaction among the indicator, the receptor, and the analyte, and (C) a self-assembled chemosensing system based on a competitive reaction among the indicator (and target binding unit), the optical manipulator, and the analyte. Figure 2 was adapted from [17] (© 2023 Y. Sasaki & T. Minami. *ChemNanoMat* published by Wiley-VCH GmbH, distributed under the terms of the Creative Commons Attribution 4.0 International License, https://creativecommons.org/licenses/by/4.0).

tors. To induce recognizable optical responses, molecular dynamics during the association and dissociation of color manipulators are significant [36].

Dynamic covalent bonds are key motifs that contribute to the formation of self-assembled chemosensors and analyte detection [45,46]. Phenylboronic acid derivatives have been widely used as the building blocks for versatile supramolecular architectures [47-49]. The inherent reversibility derived from dynamic covalent bonds endows unique functions to the self-assembled structures. In the field of analytical chemistry, beneficial molecular behavior based on boronate esterification has been applied to reversible and continuous analyte detection [48]. In conventional chemosensor designs, phenylboronic acid derivatives are widely used as receptor units for analytes with cis-diol moieties [47-49]. Also, the favorable binding affinity of phenylboronic acid derivatives enables the formation of ensembles with indicators bearing cis-diol units [50-52].

Catechol derivatives demonstrate favorable metal-ion recognition abilities, owing to the presence of two adjacent hydroxy groups [53]. The optical properties of catechol derivatives correspond to the protonation and deprotonation forms [54]. The coordination with metal ions promotes the deprotonation of catechol derivatives from neutral structures [53]. Herein, we focus on phenylboronic acid as an optical manipulator of catechol derivatives that act as indicators and binding sites for metal ions and discuss the usability of this combination in the simultaneous detection of metal ions.

Dynamic covalent bond-based chemosensors for metal ion detection in solution states

In this chemosensor design, catechol derivatives (i.e., alizarin red S (**1**), bromopyrogallol red (**2**), pyrogallol red (**3**), and pyrocatechol violet (**4**)) and a phenylboronic acid derivative (i.e., 3-nitrophenylboronic acid (**5**)) are employed (Figure 3) [13,20]. These building blocks are assembled through boronate esterification, which induces an optical change. For example, the catechol dye **1** showed blueshifts in the UV–vis absorption spectra with an increase in concentration of **5**, which supported the spontaneous formation of a boronate ester (Figure 4A). The nitrophenyl moiety acting as an electron-withdrawing group of **5** increases the Lewis acidity of boronic acid and facilitates the formation of boronate esters [11]. Meanwhile, the colorimetric ensemble of **1** and **5** exhibited redshifts in the UV–vis absorption spectra in the presence of a target metal ion (Ni^{2+}). The optical changes suggested the coordination between **1** and the metal ion, along with the release of **5**, according to a competitive reaction among **1**, **5**, and the metal ion (Figure 4B). In this sensing approach, the catechol derivative served as the binding site for metal ions, resulting in a unique spectral profile. Consequently, this method induces versatile optical patterns beyond simple signal recovery and, thus, enables simultaneous discrimination of various metal ions even with a small number of chemosensor elements.

Scheme of pattern recognition-driven chemical sensing

The process of simultaneous detection comprises several steps, namely, design and preparation of chemosensors, recording chemosensor responses to analytes, collection and preparation of input data, data processing using chemometric techniques, and visualization of chemical information (Figure 5) [36]. The optical responses of chemosensors and their arrays are acquired using spectrophotometers and portable recording apparatuses. The recorded optical responses as spectral profiles and digital images are summarized into a data matrix, according to the categories of types of chemosensor elements, analytes, and their concentrations. To validate the reproducibility of the sensing performance, replicate measurements are carried out. Therefore, the data matrix contains multidimensional chemical information, which can be processed using chemometric methods to classify and predict chemical information and to visualize the results as two- and three-dimensional outputs [39].

Herein, the assays are categorized into three types, namely, qualitative (i.e., discrimination among analyte types), semiquan-

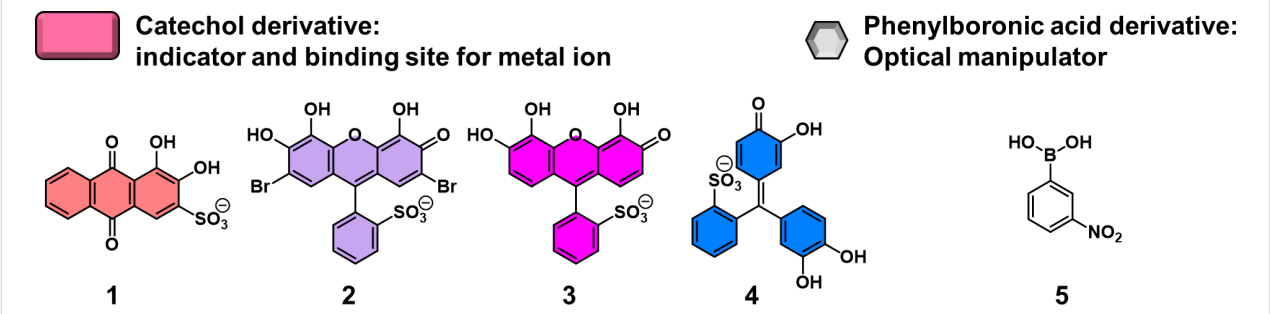

Figure 3: Chemical structures of catechols **1**–**4** and phenylboronic acid derivative **5**.

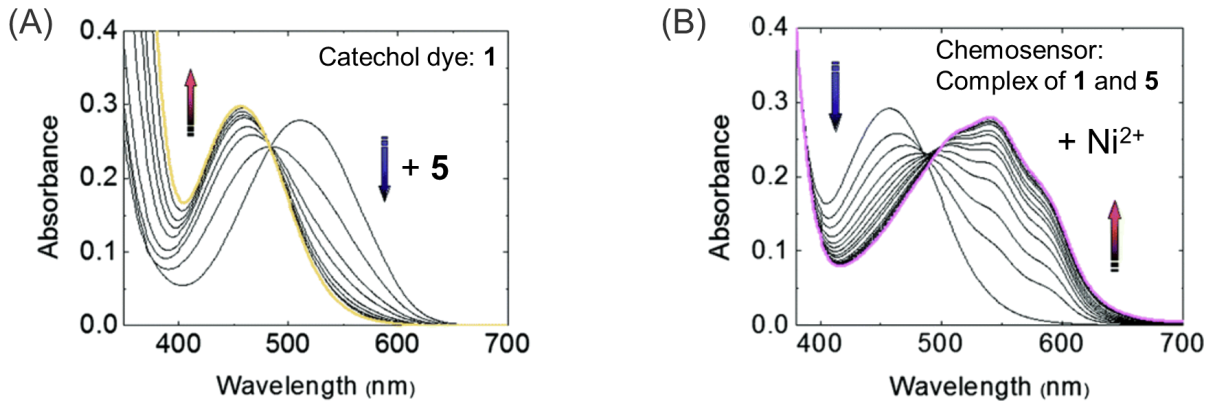

Figure 4: Colorimetric changes of a catechol dye **1** derived from (A) association with **5** through boronate esterification and (B) competitive coordination with Ni^{2+} in the presence of **5** in aqueous media. Figure 4, panels A and B were used with permission of The Royal Society of Chemistry, from [13] ("A molecular self-assembled colorimetric chemosensor array for simultaneous detection of metal ions in water" by Y. Sasaki et al., *Chem. Commun.*, Vol. 53, Issue 49, © 2017). This content is not subject to CC BY 4.0.

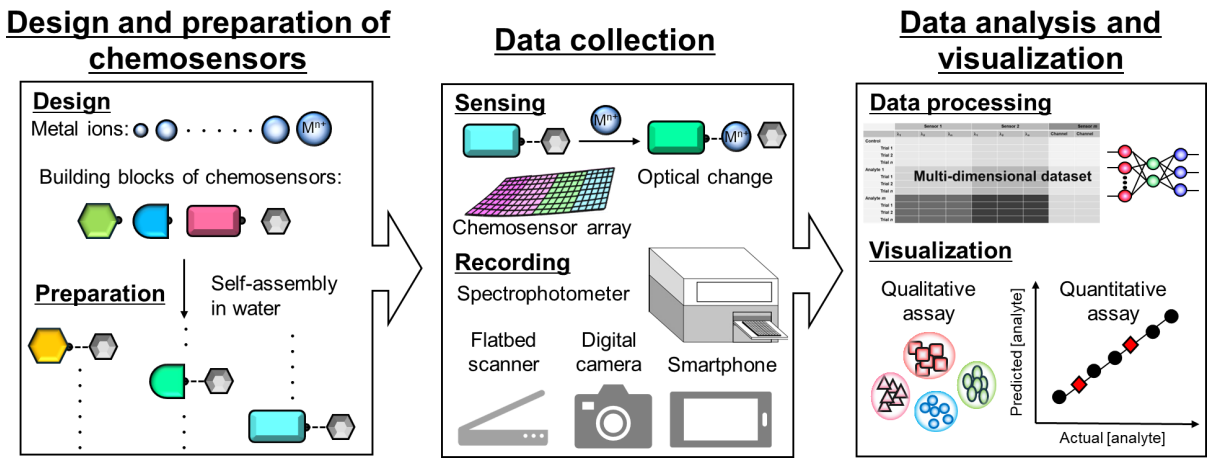

Figure 5: Conceptual scheme for pattern recognition-driven chemical sensing.

titative (i.e., discrimination among analyte types and concentration levels), and quantitative detection (i.e., prediction of unknown analytes and their concentrations in real samples) [36]. Next, data processing is performed using supervised and unsupervised methods, depending on the purpose of the analysis. Unsupervised methods include principal component analysis (PCA) and hierarchical clustering analysis (HCA), while supervised methods include linear discriminant analysis (LDA), support vector machine (SVM), and artificial neural network (ANN). The details of each method have already been summarized in previous reviews [39]. In this perspective, simultaneous detection using LDA and SVM is introduced as an example [39]. LDA reduces the dimensionality of the input data and classifies each component based on its differences [39]. In the following sections, LDA is introduced for qualitative discrimination, whereas SVM is used for quantitative assays [55]. Thus, the analytical method can be used for quantitative assays in complicated media, such as mixtures of analytes and real samples in the presence of interfering species.

Colorimetric chemosensor arrays for qualitative detection of eleven metal ions

To explore the potential of colorimetric self-assembled chemosensors, the three catechol dyes **1**–**3** and the color manipulator **5** were selected as components of an array for the simultaneous discrimination of eleven types of metal ions (i.e., Pb^{2+}, Cu^{2+}, Zn^{2+}, Ni^{2+}, Cd^{2+}, Co^{2+}, Fe^{2+}, Hg^{2+}, Al^{3+}, Ga^{3+}, and Ca^{2+}) [13]. As described in Figure 6A, the various colorimetric patterns were obtained on an array, according to the combination of the colorimetric ensembles and target metal ions. Importantly, the magnitude of the color changes of the catechol dyes in response to the metal ions was significant in the presence of

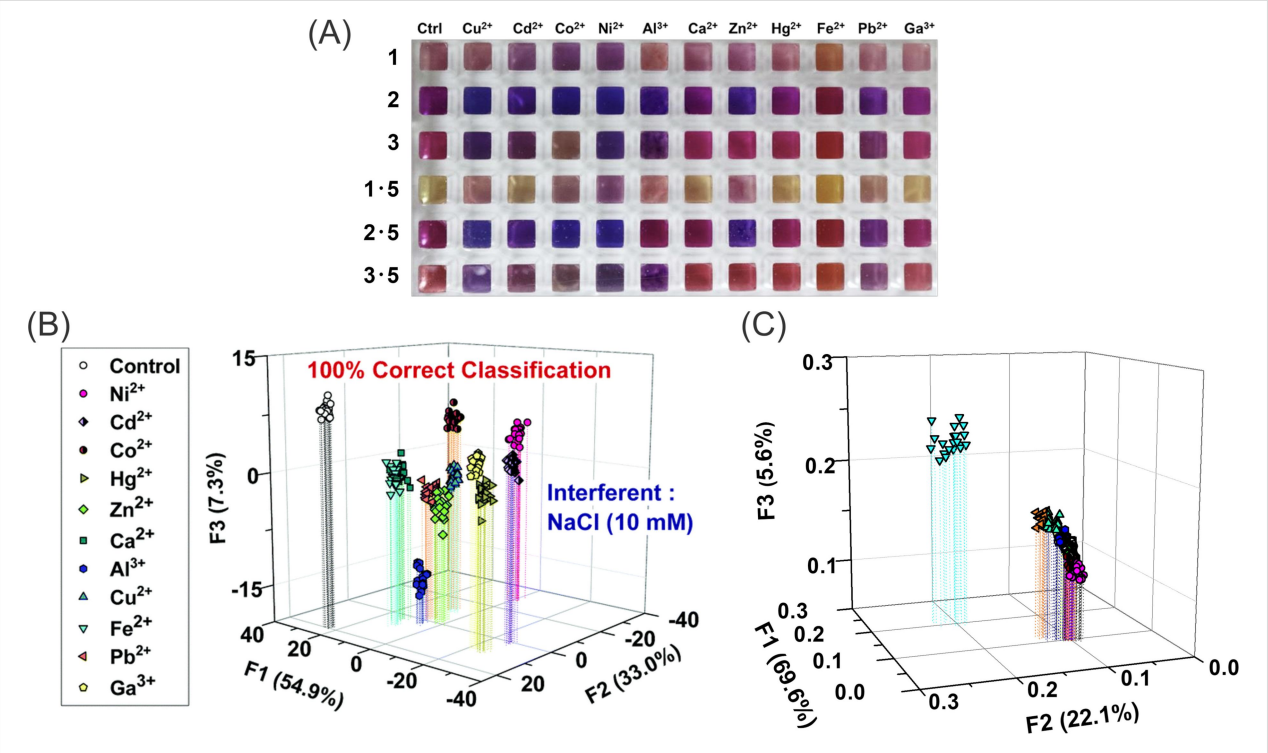

Figure 6: (A) Colorimetric patterns of a stand-alone dye array and the self-assembled chemosensor array in the presence or absence of metal ions. LDA canonical score plots for the qualitative assay of eleven metal ions using (B) the self-assembled chemosensor array and (C) the stand-alone dye array in aqueous media. Figure 6, panels A and B were used with permission of The Royal Society of Chemistry, from [13] ("A molecular self-assembled colorimetric chemosensor array for simultaneous detection of metal ions in water" by Y. Sasaki et al., *Chem. Commun.*, Vol. 53, Issue 49, © 2017). This content is not subject to CC BY 4.0. Figure 6, panel (C) was reproduced with permission from [56]. © 2018 Institute of Industrial Science, The University of Tokyo. This content is not subject to CC BY 4.0.

5, unlike without the color manipulator (i.e., stand-alone dye array). Indeed, the qualitative detection with 100% correct classification was achieved for eleven types of metal ions, even with excess amounts of sodium chloride (NaCl) (Figure 6B). In this assay, the input data for LDA were constructed using UV–vis absorption spectra of chemosensors upon analyte addition. The dimensionality of the input data depends on the number of chemosensors, analytes, and replicate measurements, which is decreased using LDA. Each axis (i.e., factor, F) corresponds to the contribution derived from the multidimensional colorimetric response dataset [39]. The stand-alone dye array did not show accurate discrimination of the same metal ions (Figure 6C) [56]. Overall, the spontaneous preparation approaches using the catechol and the phenylboronic acid derivatives suggested the feasibility of simultaneous detection of metal ions in solution states, based on cross-reactivity and reversibility of self-assembled chemosensors.

Solid-state chemosensor array device toward on-site metal ion detection

Based on the concept described above, a paper-based chemosensor array device was fabricated by printing self-assembled chemosensor elements onto paper substrates. To demonstrate the concept of cross-scale design, this section introduces a paper-based chemosensor array device embedded with the colorimetric ensembles that have already been evaluated in solution states. Herein, the key aspect of this concept is the retention of sensing performance of the self-assembled chemosensors even on the paper substrates.

Design and fabrication of the paper-based chemosensor array device

The uniformity of the sensing layer significantly affects the reproducibility and accuracy of analyte detection. Therefore, a printed pattern with 96 microwells was designed to avoid coffee ring effects [57]. Device designs (well design and area length and width), printing conditions and process (printing cycles of chemosensor inks), and sensing process (analyte solution volume) were optimized using a central composite design [58].

The selection of appropriate paper substrates also plays a significant role in reproducible sensing [59]. The mechanical properties of paper substrates depend on their thickness, pore size, and liquid absorbability [21]. In particular, the thickness of the substrates influences the magnitude of optical changes [60]. In addition, the fiber structures of paper substrates effec-

tively contribute to the high dispersion of chemosensor elements [28].

The fabrication process in Figure 7A begins with patterning a hydrophobic layer using an office wax printer. The printed wax layer melts on a hot plate during annealing. Next, an inkjet printer is employed to deposit chemosensor solutions onto predefined regions of the paper substrate. The fiber structures of paper substrates contribute to highly dispersed chemosensor elements, resulting in uniform solid-state sensing layers (Figure 7B). Upon exposure to metal ions in aqueous solutions, the immobilized chemosensors interact with the analytes and induce optical changes on the paper substrate. These optical patterns are rapidly recorded using portable devices. Subsequently, the captured digital photographs are processed using imaging analysis to extract color information (e.g., RGB values) and further analyzed using pattern-recognition methods. Indeed, each chemosensor on the paper device showed different colorimetric responses to metal ions, indicating the fingerprint-like patterns containing multidimensional optical information.

Solid-state simultaneous detection of metal ions

Next, the 96-well microtiter paper-based chemosensor array device embedded with four types of colorimetric ensembles using building blocks **1**–**5** was employed for the qualitative discrimination of nine types of metal ions. Although the same sensor molecules were applied, the sensing environments are significantly different in solution and in the solid state. Therefore, in contrast to solution-based chemosensors, an additional ensemble made of **4** and **5** was included in the chemosensor library as an array component to increase optical response patterns. The obtained colorimetric changes on the device were rapidly recorded using a flatbed scanner [20]. The fabricated device demonstrated 100% correct classification of nine types of metal ions (Figure 8B). From the sensitivity aspect, the detectable ranges of the paper-based device were comparable to those of the solution-based chemosensor array. The concept can also be extended to polymer-based chemosensor elements. In a previous study, a polythiophene derivative immobilized chemosensor array on a paper substrate achieved highly sensitive detection of metal ions at tens of parts per billion levels, which was comparable to the detection range of an analytical method based on a stationary spectrophotometer [28].

Applicability of the paper-based chemosensor array to real-sample analysis

Herein, the usability of the paper-based chemosensor array device in real-sample analysis is introduced [20]. To realize the concept of cross-scale design, the sensor performance of chemosensor elements in solution states should be maintained or improved on the paper substrates. In environmental assessment, metal ion levels in river water indicate the state of ecological systems [1,2]. The colorimetric responses in the presence of interferents show non-linearity. Therefore, a powerful machine-learning method, SVM, was employed to build a linear calibration line from datasets constructed by color channels. Spike-and-recovery tests toward Zn^{2+} and Cu^{2+} demonstrated reliable analytical performance with recovery rates of 89–125%, even without sample purification (Figure 8C,D). To compare the sensing performance of the paper-based analytical device, recent paper-based colorimetric sensor devices for metal ion detection are summarized in Table 1. As shown, many paper-based analytical devices enable real-sample analysis with simple operation and minimal sample pretreatment. Indeed, the

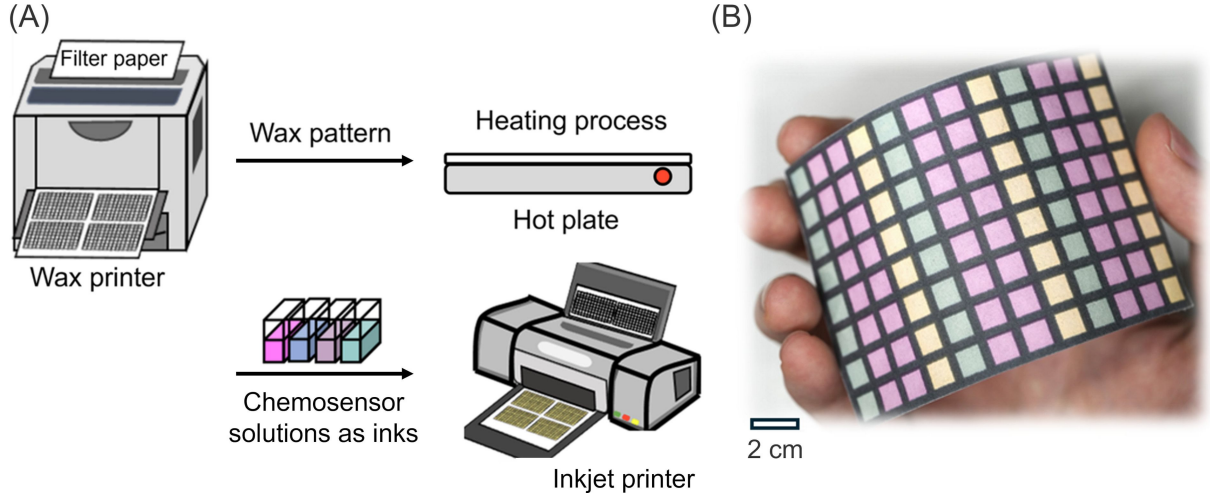

Figure 7: (A) Schematic of device fabrication using office printers and apparatus. (B) Photograph of the 96-well microtiter paper-based chemosensor array device. Figure 7 was adapted from [20] (© 2023 Y. Sasaki et al., distributed under the terms of the Creative Commons Attribution 4.0 International License, https://creativecommons.org/licenses/by/4.0).

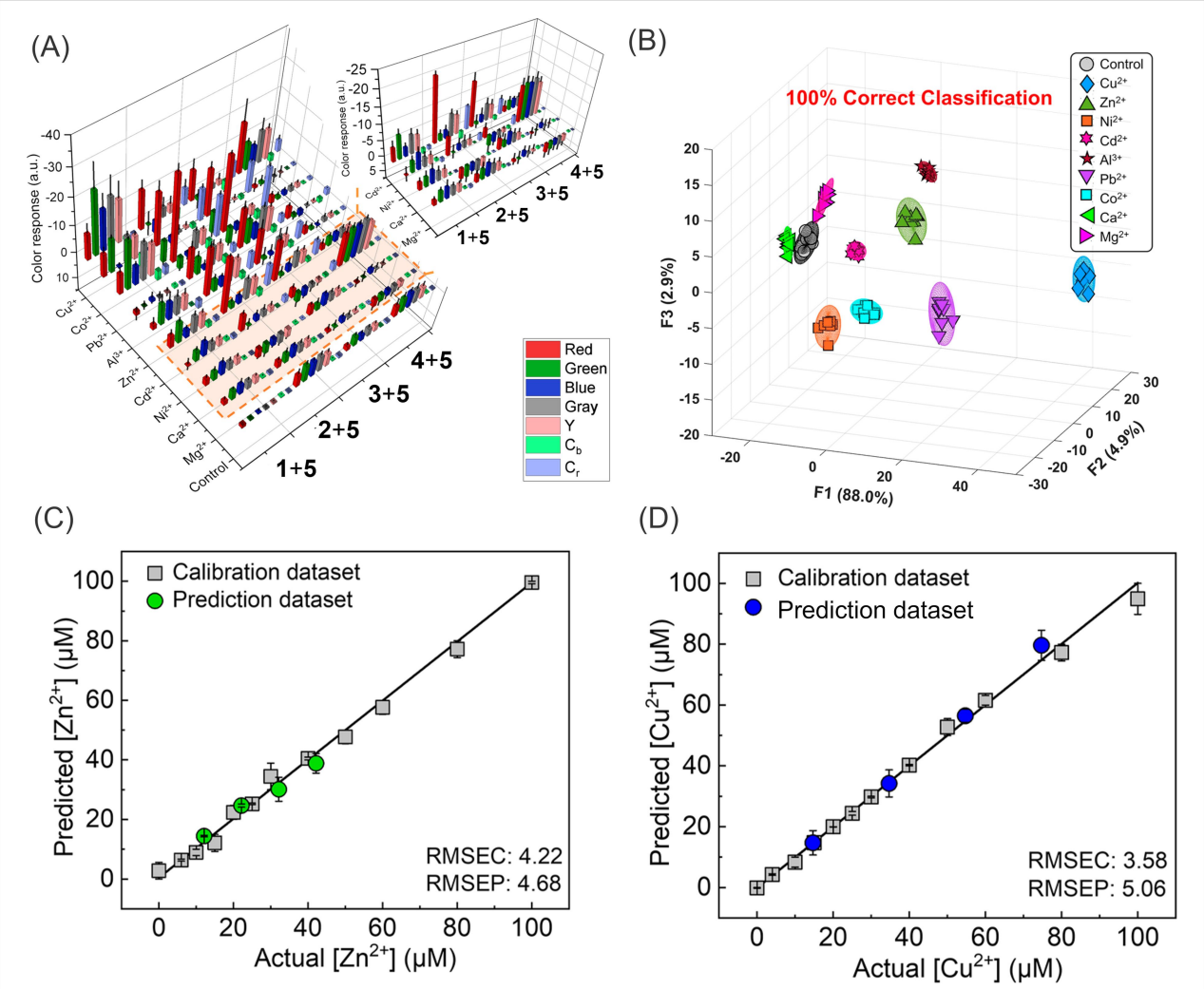

Figure 8: (A) Color response profile of the paper-based chemosensor array device upon adding target metal ions. (B) LDA canonical score plot for the qualitative assay of nine types of metal ions using the paper-based chemosensor array device. Results of the SVM regression for (C) Zn^{2+} and (D) Cu^{2+} in a river water sample. The values of the root-mean-square errors of calibration (RMSEC) and prediction (RMSEP) suggest the accuracy of the established model and prediction results. Figure 8, panels A–D were reproduced from [20] (© 2023 Y. Sasaki et al., distributed under the terms of the Creative Commons Attribution 4.0 International License, https://creativecommons.org/licenses/by/4.0).

sensor performance from the viewpoint of usability and applicability is beyond that of solution-based chemosensors in metal ion sensing.

Conclusion

In this perspective, we described the concept of cross-scale design for metal ion detection by integrating self-assembled chemosensors with solid-state analytical devices. Self-assembled chemosensor systems based on dynamic covalent bonds between catechol and phenylboronic acid derivatives provide a versatile platform for the spontaneous preparation of chemosensor elements without extensive synthetic effort. The reversible formation of boronate esters enables cross-reactive sensing behavior, providing fingerprint-like response patterns for various metal ions and their concentrations. By applying chemometric methods, multidimensional chemical information can be visualized qualitatively and quantitatively.

To address the challenges of metal ion analysis outside laboratories, paper-based platforms are attractive owing to their compatibility with office-printing technologies and portable imaging tools. Importantly, the paper-based chemosensor array device demonstrated reliable analytical performance in river water samples without the need for stationary analytical instruments or sample preparation.

The combination of molecular self-assembly, pattern-recognition sensing, and printable analytical devices provides a promising strategy for bridging molecular sensing systems in solution and solid-state analytical devices toward practical metal ion

Table 1: Comparison of representative paper-based colorimetric sensing devices for metal-ion detection.

Probe/device	Medium	LOD (μM)[a]	Key metrics	Ref.
plug-and-play μPAD with colorimetric reagents (bathophenanthroline, dimethylglyoxime, and bathocuproine)	river water	Fe^{2+} 1.79, Ni^{2+} 5.11, Cu^{2+} 3.15	recovery rate (76–121%) agrees with AAS	[61]
inkjet-printed paper optode	drinking and environmental water	Pb^{2+} N.R.[b]; dynamic range 1–10	quick sensor response (<5 min)	[62]
mesoporous silica nanosphere-coated paper chemosensor	water	Cd^{2+} 0.22, Co^{2+} 0.28, Ni^{2+} 0.44, Fe^{3+} 0.54	reusability (for five cycles) after chelate treatment	[63]
silica nanoparticle-modified rhodamine B paper strip	drinking water	Cu^{2+} 11.0	sensor performance validated by ICP-OES	[64]
imidazole–dithiocarbamate derivative-coated tissue-paper strip	water samples	Cu^{2+} 0.0151, Hg^{2+} 1.17	different optical properties depending on the target metal ions	[65]
chemosensor array device functionalized with ensembles of catechol dyes and a phenylboronic acid derivative	river water	Cu^{2+} 2.36, Zn^{2+} 2.60, Ni^{2+} 4.77	qualitative and quantitative assays in metal-ion mixtures; recovery rate: 89–125% for Zn^{2+} and Cu^{2+} in river water	[20]
capillary-flow microfluidic paper device functionalized with colorimetric reagents (dimethylglyoxime, bathocuproine, and bathophenanthroline)	water	Ni^{2+} 34.1, Cu^{2+} 4.72, Fe^{3+} 19.7	recovery rates of 80–110% for >90% of collected samples	[66]
sodium rhodizonate-attached paper device	drinking, tap, and Ilam platform water samples	Ba^{2+} 26.5, Sr^{2+} 54.2	smartphone-assisted assay applying a masking strategy	[67]
bi-ligand cobalt-MOF nanozyme with 3,3′,5,5′-tetramethylbenzidine/H_2O_2 chromogenic system	environmental water	Cu^{2+} 0.130	smartphone-assisted sensor for on-site analysis	[68]
paper device immobilized with eriochrome black T (EBT) and bromothymol blue (BTB)	aqueous medium	Pb^{2+} (BTB) 29.0, Pb^{2+} (EBT) 86.9	high selectivity against other ions; thermal stability at 25–90 °C	[69]
dithizone colorimetric reagent immobilized on paper using a polyvinyl chloride matrix plasticized with dibutyl phthalate	water	Pb^{2+} 6.08, Cd^{2+} 0.890	rapid detection (150 s for Pb^{2+} and 60 s for Cd^{2+})	[70]
naphthylamine–quinolinol azo chemosensor-attached test strip	water and food samples[c]	Cd^{2+} 0.0262	reusability for six cycles with a chelate agent	[71]
dual-sided capillary microfluidic paper device immobilized with colorimetric reagents (dimethylglyoxime, bathocuproine, and bathophenanthroline)	river, tap, pond, drinking water	Ni^{2+} 22.1, Fe^{3+} 5.37, Cu^{2+} 3.15	recovery rate: 86–112%; stable for >4 weeks	[72]
paper strips using chromogens (cuprizone, 1,5-diphenylcarbazide, zincon monosodium salt, and 1-(2-pyridylazo)-2-naphthol)	environmental water	Cu^{2+} 4.72, Cr(VI) 5.00, Zn^{2+} 11.0, Mn^{2+} 5.10	comparable sensing performance with AAS	[73]

[a]LOD values were converted to "μM" for direct comparison. Reported ppm values were treated as "mg·L^{-1}" for dilute aqueous samples. Atomic weights used for conversion were Fe 55.845, Co 58.933, Ni 58.693, Cu 63.546, Zn 65.38, Cd 112.414, Ba 137.327, Sr 87.62, Cr 51.996, Mn 54.938, Hg 200.59, and Pb 207.2 g·mol^{-1}. For Cr(VI), conversion was based on the atomic weight of Cr. [b]N.R.: not reported; the corresponding study reported a dynamic range rather than an explicit LOD. [c]Food samples included potato, mushroom, apple, carrot, corn, barley, cashew, and sunflower seeds.

assessment. We believe that such cross-scale design approaches will contribute to on-site detection of chemical species in water environments across microscopic to macroscopic scales. More broadly, the cross-scale design strategy presented here may provide a general framework for bridging molecular recognition systems into practical sensing technologies that operate across molecular, nanoscale, and device levels.

Funding

Y. S. gratefully acknowledges the financial support from the Japan Society for the Promotion of Science (JSPS) KAKENHI (Grant No. JP24K17667) and JST PRESTO (Grant No. JPMJPR23H2). T. M. thanks JSPS KAKENHI (Grant Nos. JP23H03864, JP24K01315, JP25K22200, and JP25K24718).

Author Contributions

Yui Sasaki: funding acquisition; writing – original draft. Tsuyoshi Minami: conceptualization; funding acquisition; project administration; supervision; writing – review & editing.

ORCID® iDs

Yui Sasaki - https://orcid.org/0000-0003-4185-569X
Tsuyoshi Minami - https://orcid.org/0000-0001-8331-378X

Data Availability Statement

Data sharing is not applicable as no new data was generated or analyzed in this study.

References

1. Aragay, G.; Pons, J.; Merkoçi, A. *Chem. Rev.* **2011,** *111,* 3433–3458. doi:10.1021/cr100383r
2. Malik, L. A.; Bashir, A.; Qureashi, A.; Pandith, A. H. *Environ. Chem. Lett.* **2019,** *17,* 1495–1521. doi:10.1007/s10311-019-00891-z
3. Wang, B.; Anslyn, E. V., Eds. *Chemosensors: Principles, Strategies, and Applications;* Wiley, 2011. doi:10.1002/9781118019580
4. Wang, Y.-Y.; Kong, Y.; Zheng, Z.; Geng, W.-C.; Zhao, Z.-Y.; Sun, H.; Guo, D.-S. *Beilstein J. Org. Chem.* **2019,** *15,* 1394–1406. doi:10.3762/bjoc.15.139
5. Gharibzahedi, S. M. T.; Altintas, Z. *Beilstein J. Nanotechnol.* **2025,** *16,* 2207–2244. doi:10.3762/bjnano.16.153
6. Prodi, L.; Bolletta, F.; Montalti, M.; Zaccheroni, N. *Coord. Chem. Rev.* **2000,** *205,* 59–83. doi:10.1016/s0010-8545(00)00242-3
7. Patil, A.; Salunke-Gawali, S. *Inorg. Chim. Acta* **2018,** *482,* 99–112. doi:10.1016/j.ica.2018.05.026
8. Ghosh, P.; Roy, P. *Chem. Commun.* **2023,** *59,* 5174–5200. doi:10.1039/d3cc00651d
9. Zhang, H.; Song, J.; Wang, S.; Song, Q.; Guo, H.; Li, Z. *Dyes Pigm.* **2023,** *216,* 111380. doi:10.1016/j.dyepig.2023.111380
10. Pal, R.; Das, R.; Pal, A.; Kapoor, B. S.; Kundu, K.; Thakur, A.; Mukhopadhyay, S. S.; Banerjee, P. *Microchem. J.* **2024,** *207,* 111739. doi:10.1016/j.microc.2024.111739
11. Chattopadhyay, M. K.; Mondal, A.; Hazra, A.; Tarai, S. K.; Kapoor, B. S.; Mukhopadhyay, S. S.; Sarkar, S.; Banerjee, P. *Sens. Actuators Rep.* **2024,** *8,* 100215. doi:10.1016/j.snr.2024.100215
12. Palacios, M. A.; Wang, Z.; Montes, V. A.; Zyryanov, G. V.; Anzenbacher, P., Jr. *J. Am. Chem. Soc.* **2008,** *130,* 10307–10314. doi:10.1021/ja802377k
13. Sasaki, Y.; Minamiki, T.; Tokito, S.; Minami, T. *Chem. Commun.* **2017,** *53,* 6561–6564. doi:10.1039/c7cc03218h
14. Ihde, M. H.; Tropp, J.; Diaz, M.; Shiller, A. M.; Azoulay, J. D.; Bonizzoni, M. *Adv. Funct. Mater.* **2022,** *32,* 2112634. doi:10.1002/adfm.202112634
15. Sasaki, Y.; Ohshiro, K.; Zhou, Q.; Lyu, X.; Tang, W.; Okabe, K.; Takizawa, S.-y.; Minami, T. *Chem. Commun.* **2023,** *59,* 7747–7750. doi:10.1039/d3cc00949a
16. Yang, R.-P.; Huang, S.-Z.; Wei, K.-N.; Tang, Q.; Tao, Z.; Huang, Y.; Zhao, A.-T. *Dalton Trans.* **2023,** *52,* 7279–7289. doi:10.1039/d3dt00995e
17. Sasaki, Y.; Minami, T. *ChemNanoMat* **2024,** *10,* e202300335. doi:10.1002/cnma.202300335
18. Praveen, V. K.; Vedhanarayanan, B.; Mal, A.; Mishra, R. K.; Ajayaghosh, A. *Acc. Chem. Res.* **2020,** *53,* 496–507. doi:10.1021/acs.accounts.9b00580
19. Wu, J.; Kwon, B.; Liu, W.; Anslyn, E. V.; Wang, P.; Kim, J. S. *Chem. Rev.* **2015,** *115,* 7893–7943. doi:10.1021/cr500553d
20. Sasaki, Y.; Lyu, X.; Minami, T. *Front. Chem. (Lausanne, Switz.)* **2023,** *11,* 1134752. doi:10.3389/fchem.2023.1134752
21. Mohan, B.; Sasaki, Y.; Minami, T. *Anal. Chim. Acta* **2024,** *1313,* 342741. doi:10.1016/j.aca.2024.342741
22. Wang, S.; Chen, W.-J.; Du, A.; Kou, Y.; Xu, X.; Hu, D.; Lu, Z. *Adv. Compos. Hybrid Mater.* **2025,** *8,* 260. doi:10.1007/s42114-025-01333-x
23. Zhang, Q.; Yan, J.; Ma, X.; Zhao, L.; Song, P.; Xia, L. *J. Hazard. Mater.* **2024,** *480,* 136195. doi:10.1016/j.jhazmat.2024.136195
24. Devadhasan, J. P.; Kim, J. *Sens. Actuators, B* **2018,** *273,* 18–24. doi:10.1016/j.snb.2018.06.005
25. Datta, S.; Dey, S.; Sinha, C.; Dutta, B.; Banerjee, P.; Mir, M. H. *Dalton Trans.* **2024,** *53,* 2859–2866. doi:10.1039/d3dt03939k
26. Alahmad, W.; Cetinkaya, A.; Kaya, S. I.; Varanusupakul, P.; Ozkan, S. A. *Trends Environ. Anal. Chem.* **2023,** *40,* e00220. doi:10.1016/j.teac.2023.e00220
27. Díaz-Liñán, M. C.; García-Valverde, M. T.; Lucena, R.; Cárdenas, S.; López-Lorente, A. I. *Anal. Methods* **2020,** *12,* 3074–3091. doi:10.1039/d0ay00702a
28. Sasaki, Y.; Lyu, X.; Kawashima, T.; Zhang, Y.; Ohshiro, K.; Okabe, K.; Tsuchiya, K.; Minami, T. *RSC Adv.* **2024,** *14,* 5159–5166. doi:10.1039/d3ra08429a
29. Yamada, K.; Shibata, H.; Suzuki, K.; Citterio, D. *Lab Chip* **2017,** *17,* 1206–1249. doi:10.1039/c6lc01577h
30. Geng, Z.; Miao, Y.; Zhang, G.; Liang, X. *Sens. Actuators, A* **2023,** *349,* 114056. doi:10.1016/j.sna.2022.114056
31. Sedgwick, A. C.; Brewster, J. T.; Wu, T.; Feng, X.; Bull, S. D.; Qian, X.; Sessler, J. L.; James, T. D.; Anslyn, E. V.; Sun, X. *Chem. Soc. Rev.* **2021,** *50,* 9–38. doi:10.1039/c9cs00538b
32. Geng, Y.; Peveler, W. J.; Rotello, V. M. *Angew. Chem., Int. Ed.* **2019,** *58,* 5190–5200. doi:10.1002/anie.201809607
33. Lu, X.; Suslick, K. S.; Li, Z. *Analysis Sensing* **2023,** *3,* e202200050. doi:10.1002/anse.202200050
34. Shimizu, K. D.; Stephenson, C. J. *Curr. Opin. Chem. Biol.* **2010,** *14,* 743–750. doi:10.1016/j.cbpa.2010.07.007
35. Ke, Y.; Sun, Y.; Liao, A.; Zhao, F.; Tan, Y.; Tan, C. *ACS Appl. Mater. Interfaces* **2025,** *17,* 16396–16409. doi:10.1021/acsami.4c22848
36. Sasaki, Y.; Kubota, R.; Minami, T. *Coord. Chem. Rev.* **2021,** *429,* 213607. doi:10.1016/j.ccr.2020.213607
37. Anzenbacher, P., Jr.; Liu, Y.-l.; Kozelkova, M. E. *Curr. Opin. Chem. Biol.* **2010,** *14,* 693–704. doi:10.1016/j.cbpa.2010.08.011
38. Ikeda, M.; Ochi, R.; Hamachi, I. *Lab Chip* **2010,** *10,* 3325–3334. doi:10.1039/c004908e
39. Anzenbacher, P., Jr.; Lubal, P.; Buček, P.; Palacios, M. A.; Kozelkova, M. E. *Chem. Soc. Rev.* **2010,** *39,* 3954–3979. doi:10.1039/b926220m
40. Albert, K. J.; Lewis, N. S.; Schauer, C. L.; Sotzing, G. A.; Stitzel, S. E.; Vaid, T. P.; Walt, D. R. *Chem. Rev.* **2000,** *100,* 2595–2626. doi:10.1021/cr980102w
41. Li, Z.; Askim, J. R.; Suslick, K. S. *Chem. Rev.* **2019,** *119,* 231–292. doi:10.1021/acs.chemrev.8b00226
42. Guo, C.; Sedgwick, A. C.; Hirao, T.; Sessler, J. L. *Coord. Chem. Rev.* **2021,** *427,* 213560. doi:10.1016/j.ccr.2020.213560

43. Nguyen, B. T.; Anslyn, E. V. *Coord. Chem. Rev.* **2006,** *250,* 3118–3127. doi:10.1016/j.ccr.2006.04.009
44. Hay, B. P.; Hancock, R. D. *Coord. Chem. Rev.* **2001,** *212,* 61–78. doi:10.1016/s0010-8545(00)00366-0
45. Sasaki, Y.; Kojima, S.; Hamedpour, V.; Kubota, R.; Takizawa, S.-y.; Yoshikawa, I.; Houjou, H.; Kubo, Y.; Minami, T. *Chem. Sci.* **2020,** *11,* 3790–3796. doi:10.1039/d0sc00194e
46. You, L. *Chem. Commun.* **2023,** *59,* 12943–12958. doi:10.1039/d3cc04022d
47. Nishiyabu, R.; Kubo, Y.; James, T. D.; Fossey, J. S. *Chem. Commun.* **2011,** *47,* 1124–1150. doi:10.1039/c0cc02921a
48. Bian, Z.; Liu, A.; Li, Y.; Fang, G.; Yao, Q.; Zhang, G.; Wu, Z. *Analyst* **2020,** *145,* 719–744. doi:10.1039/c9an00741e
49. António, J. P. M.; Roque, I. L.; Santos, F. M. F.; Gois, P. M. P. *Acc. Chem. Res.* **2025,** *58,* 673–687. doi:10.1021/acs.accounts.4c00691
50. Springsteen, G.; Wang, B. *Chem. Commun.* **2001,** 1608–1609. doi:10.1039/b104895n
51. Kubo, Y.; Ishida, T.; Kobayashi, A.; James, T. D. *J. Mater. Chem.* **2005,** *15,* 2889–2895. doi:10.1039/b501243k
52. Tomsho, J. W.; Benkovic, S. J. *J. Org. Chem.* **2012,** *77,* 2098–2106. doi:10.1021/jo202250d
53. Zhang, L.; Dong, S.; Zhu, L. *Chem. Commun.* **2007,** 1891–1893. doi:10.1039/b618413h
54. Carta, L.; Biczysko, M.; Bloino, J.; Licari, D.; Barone, V. *Phys. Chem. Chem. Phys.* **2014,** *16,* 2897–2911. doi:10.1039/c3cp50499a
55. Minami, T.; Esipenko, N. A.; Zhang, B.; Kozelkova, M. E.; Isaacs, L.; Nishiyabu, R.; Kubo, Y.; Anzenbacher, P., Jr. *J. Am. Chem. Soc.* **2012,** *134,* 20021–20024. doi:10.1021/ja3102192
56. Sasaki, Y.; Minami, T. *Seisan Kenkyu* **2018,** *70,* 193–196. doi:10.11188/seisankenkyu.70.193
57. Lyu, X.; Hamedpour, V.; Sasaki, Y.; Zhang, Z.; Minami, T. *Anal. Chem. (Washington, DC, U. S.)* **2021,** *93,* 1179–1184. doi:10.1021/acs.analchem.0c04291
58. Hamedpour, V.; Oliveri, P.; Malegori, C.; Minami, T. *Sens. Actuators, B* **2020,** *322,* 128571. doi:10.1016/j.snb.2020.128571
59. Xu, Y.; Bonizzoni, M. *Analyst* **2020,** *145,* 3505–3516. doi:10.1039/d0an00137f
60. Pratiwi, R.; Septyani, R. N.; Febriany, R.; Saputri, F. A.; Nuwarda, R. F. *Int. J. Anal. Chem.* **2019,** *2019,* 4682839. doi:10.1155/2019/4682839
61. Silva-Neto, H. A.; Cardoso, T. M. G.; McMahon, C. J.; Sgobbi, L. F.; Henry, C. S.; Coltro, W. K. T. *Analyst* **2021,** *146,* 3463–3473. doi:10.1039/d1an00176k
62. Cui, Y.; Wang, R.; Brady, B.; Wang, X. *Anal. Bioanal. Chem.* **2022,** *414,* 7585–7595. doi:10.1007/s00216-022-04286-y
63. El-Sewify, I. M.; Radwan, A.; Azzazy, H. M. E.-S. *RSC Adv.* **2023,** *13,* 6433–6441. doi:10.1039/d3ra00369h
64. Sannok, T.; Wechakorn, K.; Jantra, J.; Kaewchoay, N.; Teepoo, S. *Anal. Bioanal. Chem.* **2023,** *415,* 4703–4712. doi:10.1007/s00216-023-04754-z
65. Thangaraj, B.; Ponram, M.; Ranganathan, S.; Sambath, B.; Cingaram, R.; Iyer, S. K.; Natesan Sundaramurthy, K. *RSC Adv.* **2023,** *13,* 26023–26030. doi:10.1039/d3ra03764a
66. Aryal, P.; Brack, E.; Alexander, T.; Henry, C. S. *Anal. Chem. (Washington, DC, U. S.)* **2023,** *95,* 5820–5827. doi:10.1021/acs.analchem.3c00378
67. Ezoji, H.; Neshati, J.; Esmaeili, N. *J. Iran. Chem. Soc.* **2024,** *21,* 2713–2723. doi:10.1007/s13738-024-03103-w
68. Amalraj, A.; Ayyanu, R.; Pavadai, R.; Govindaraj, T. S.; Aham, E. C.; Li, X.; Deng, Y.; Zhang, Z. *J. Environ. Chem. Eng.* **2024,** *12,* 113522. doi:10.1016/j.jece.2024.113522
69. Poovadichalil, N. M.; Ullah, A.; Maurya, M. R.; Hasan, A.; Sadasivuni, K. K. *Int. J. Environ. Sci. Technol.* **2025,** *22,* 15467–15478. doi:10.1007/s13762-025-06636-6
70. Solhtalab, M.; Majdinasab, M.; Zarei, S.; Majdinasab, E. *J. Hazard. Mater. Adv.* **2025,** *19,* 100867. doi:10.1016/j.hazadv.2025.100867
71. Mousavi, S. H.; Mohammadi, A.; Zanjanchi, M. A.; Fallah Moafi, H. *Anal. Methods* **2025,** *17,* 9365–9380. doi:10.1039/d5ay01326g
72. Punnoy, P.; Aryal, P.; Hefner, C. E.; Brack, E.; Rodthongkum, N.; Potiyaraj, P.; Henry, C. S. *Anal. Chim. Acta* **2025,** *1356,* 344031. doi:10.1016/j.aca.2025.344031
73. Malik, S.; Singh, J.; Umar, A.; Ibrahim, A. A.; Baskoutas, S. *J. Photochem. Photobiol., A* **2026,** *471,* 116675. doi:10.1016/j.jphotochem.2025.116675

License and Terms